


## Petrogenesis of Miller Range 07273, a new type of anomalous melt breccia: Implications for impact effects on the H chondrite asteroid

Alex M. RUZICKA<sup>1,\*</sup> , Melinda HUTSON<sup>1</sup>, Jon M. FRIEDRICH<sup>2,3</sup>, Mark L. RIVERS<sup>4</sup>, Michael K. WEISBERG<sup>3,5</sup>, Denton S. EBEL<sup>3</sup>, Karen ZIEGLER<sup>6</sup>, Douglas RUMBLE III<sup>7</sup>, and Alyssa A. DOLAN<sup>2,8</sup>

<sup>1</sup>Cascadia Meteorite Laboratory, Department of Geology, Portland State University, 1721 SW Broadway, Portland, Oregon 97207, USA

<sup>2</sup>Department of Chemistry, Fordham University, 441 East Fordham Road, Bronx, New York 10458, USA

<sup>3</sup>Department of Earth and Planetary Sciences, American Museum of Natural History, 79th Street at Central Park West, New York City, New York 10024, USA

<sup>4</sup>Consortium for Advanced Radiation Sources, University of Chicago, Argonne, Illinois 60439, USA

<sup>5</sup>Department of Physical Sciences, Kingsborough College and Graduate School of the City University of New York, Brooklyn, New York 11235, USA

<sup>6</sup>Institute of Meteoritics, University of New Mexico, Albuquerque, New Mexico 87131, USA

<sup>7</sup>Geophysical Laboratory, Carnegie Institution of Washington, 5251 Broad Branch Road NW, Washington, D.C. 20015, USA

<sup>8</sup>Present address: Georgetown Law Center, 600 New Jersey Ave., NW, Washington, D.C. 20001, USA

\*Corresponding author. E-mail: ruzickaa@pdx.edu

(Received 06 December 2016; revision accepted 11 May 2017)

---

**Abstract**—Miller Range 07273 is a chondritic melt breccia that contains clasts of equilibrated ordinary chondrite set in a fine-grained (<5 μm), largely crystalline, igneous matrix. Data indicate that MIL was derived from the H chondrite parent asteroid, although it has an oxygen isotope composition that approaches but falls outside of the established H group. MIL also is distinctive in having low porosity, cone-like shapes for coarse metal grains, unusual internal textures and compositions for coarse metal, a matrix composed chiefly of clinoenstatite and omphacitic pigeonite, and troilite veining most common in coarse olivine and orthopyroxene. These features can be explained by a model involving impact into a porous target that produced brief but intense heating at high pressure, a sudden pressure drop, and a slower drop in temperature. Olivine and orthopyroxene in chondrule clasts were the least melted and the most deformed, whereas matrix and troilite melted completely and crystallized to nearly strain-free minerals. Coarse metal was largely but incompletely liquefied, and matrix silicates formed by the breakdown during melting of albitic feldspar and some olivine to form pyroxene at high pressure (>3 GPa, possibly to ~15–19 GPa) and temperature (>1350 °C, possibly to ≥2000 °C). The higher pressures and temperatures would have involved back-reaction of high-pressure polymorphs to pyroxene and olivine upon cooling. Silicates outside of melt matrix have compositions that were relatively unchanged owing to brief heating duration.

---

### INTRODUCTION

Miller Range 07273 (MIL 07273 or simply MIL) was initially classified as a shock-blackened H5 chondrite with anomalously low FeO, possibly another member of so-called low-FeO chondrites (Weisberg et al. 2010). Such chondrites resemble but

differ from other ordinary chondrites in having lower Fa contents in olivine and lower Fs contents in low-Ca pyroxene, and possibly differ in other ways (Wasson et al. 1993; McCoy et al. 1994; Russell et al. 1998; Troiano et al. 2011). The origin of these meteorites and their association with ordinary chondrites are uncertain.

Our studies of MIL 07273 suggest that it is not a low-FeO chondrite and that it likely formed on the H group parent body, although it does have anomalous oxygen isotopic composition. Moreover, a significant feature of MIL is that it is a matrix-supported impact melt breccia (clasts set within a melt matrix). Chondritic melt breccias are relatively uncommon and have not been widely recognized. For example, among all 47,642 named ordinary chondrites, melt breccias comprise only ~0.13% of H, ~0.22% of L, and ~0.23% of LL chondrites (*Meteoritical Bulletin Database*, 2016). In this article, we provide details on the petrogenesis of MIL 07273 as a representative of an apparently new type of chondritic melt breccia. Our data provide information on the nature of impact processes affecting asteroidal bodies to produce a distinctive rock type, including details pertaining to melting, brecciation, deformation, chemical reaction, pressure-temperature evolution, and thermal history.

## METHODS

We used a variety of techniques to study MIL 07273, details of which are provided in Data S1, Table S1, and Table S2 in the supporting information. In brief, we used optical microscopy (OM), electron microprobe analysis (EMPA), scanning electron microscopy (SEM), and electron back scatter diffraction (EBSD) to study a thin section (MIL 07273,12) at Portland State University and at the American Museum of Natural History for shock stage, X-ray mapping, modal analysis, quantitative phase chemistry, and crystallography. Aliquots of two bulk samples (MIL 07273,6 and 07273,10) were used for  $\mu$ CT 3-D study at the Advanced Photon Source in Argonne, for whole-rock oxygen isotopic analysis at the University of New Mexico and Carnegie Institution in Washington, and for elemental analysis at Fordham University.

## RESULTS

### Bulk Oxygen Isotope Composition

Oxygen isotope results from two independent laboratories are shown in Table 1 and Fig. 1. Although  $\delta^{18}\text{O}$  values of MIL 07273 place it in a region defined by H chondrites,  $\Delta^{17}\text{O}$  values are too high for H chondrites and are more similar to L chondrites (Fig. 1). Thus, the oxygen isotope composition of MIL 07273 does not fall within the standard fields of H or L chondrite. However, the O-isotopic composition of MIL more closely resembles H and L chondrites than any other meteorite class.

Table 1. Whole rock oxygen isotope analysis results for MIL 07273<sup>a</sup>.

	$\Delta^{17}\text{O}$ (‰)	$\delta^{17}\text{O}$ (‰)	$\delta^{18}\text{O}$ (‰)
MIL 07273,6	1.073	3.233	4.106
MIL 07272,6	1.085	3.269	4.152
MIL 07273,10	1.088	3.161	3.927
MIL 07273,10	1.128	2.957	3.464
MIL 07273,10	1.082	3.173	3.961
MIL 07273 mean	$1.09 \pm 0.02$	$3.16 \pm 0.12$	$3.92 \pm 0.27$

<sup>a</sup>The ,6 subsamples were analyzed at the Geophysical Laboratory and represent the average of two determinations each; the ,10 subsamples were analyzed at UNM. Mean and errors ( $\pm 1$  standard deviation) are based on five replicate analyses.

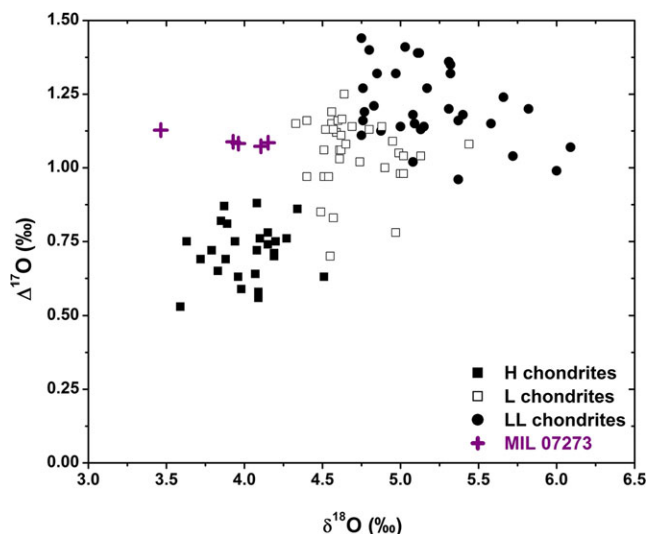


Fig. 1.  $\delta^{18}\text{O}$  versus  $\Delta^{17}\text{O}$  ( $=\delta^{17}\text{O} - 0.52 \delta^{18}\text{O}$ ) plot of oxygen isotopic compositions in MIL 07273 (this work) compared with other ordinary chondrites (Clayton et al. 1991). (Color figure can be viewed at [wileyonlinelibrary.com](http://wileyonlinelibrary.com).)

### Bulk Elemental Composition

Elemental analysis results presented in Table 2 are means weighted by the sample sizes (see Data S1). Figure 2 shows CI chondrite and Mg normalized elemental analysis results for 51 major, minor, and trace elements in MIL 07273. Kallemeyn et al. (1989) demonstrated that ordinary chondrites have mean CI chondrite- and Mg-normalized refractory lithophile abundances of ~0.9. This matches the abundances of MIL 07273 (Fig. 2a; Zr-Ba,  $n = 29$  elements). H, L, and LL chondrites show respective average CI chondrite- and Mg-normalized refractory siderophile values progressively decreasing from ~1.1, ~0.75, and ~0.6. MIL 07273 has a clear H chondrite pattern with a mean siderophile abundance of  $1.19 \pm 0.10$  (Fig. 2b, Re-Pd,  $n = 9$ ). Moderately volatile elements in ordinary

Table 2. Abundances of 51 elements in MIL 07273 determined by ICP-MS. RSD is the relative standard deviation in eight replicate analyses and largely reflects sample heterogeneity.

Element	Conc.	Value	Error (%RSD)
Li	$\mu\text{g g}^{-1}$	1.5	11
Na	$\text{mg g}^{-1}$	7.1	6
Mg	$\text{mg g}^{-1}$	137.4	5
Al	$\text{mg g}^{-1}$	11.0	5
Ca	$\text{mg g}^{-1}$	11.4	5
Sc	$\mu\text{g g}^{-1}$	7.8	12
Ti	$\mu\text{g g}^{-1}$	580	9
V	$\mu\text{g g}^{-1}$	54	21
Mn	$\text{mg g}^{-1}$	2.61	9
Fe	$\text{mg g}^{-1}$	290	20
Co	$\mu\text{g g}^{-1}$	851	32
Ni	$\text{mg g}^{-1}$	20.0	22
Cu	$\mu\text{g g}^{-1}$	85	13
Zn	$\mu\text{g g}^{-1}$	14	35
Ga	$\mu\text{g g}^{-1}$	5.4	16
As	$\mu\text{g g}^{-1}$	1.9	17
Se	$\mu\text{g g}^{-1}$	5.2	9
Rb	$\mu\text{g g}^{-1}$	2.3	9
Sr	$\mu\text{g g}^{-1}$	8.1	10
Y	$\mu\text{g g}^{-1}$	2.2	23
Zr	$\mu\text{g g}^{-1}$	7.2	17
Nb	$\text{ng g}^{-1}$	450	7
Ru	$\text{ng g}^{-1}$	1120	16
Pd	$\text{ng g}^{-1}$	930	14
Ag	$\text{ng g}^{-1}$	30	37
Sn	$\mu\text{g g}^{-1}$	160	33
Sb	$\text{ng g}^{-1}$	46	32
Te	$\text{ng g}^{-1}$	170	6
Cs	$\text{ng g}^{-1}$	5.9	13
Ba	$\mu\text{g g}^{-1}$	3.0	31
La	$\text{ng g}^{-1}$	320	30
Ce	$\text{ng g}^{-1}$	850	30
Pr	$\text{ng g}^{-1}$	130	29
Nd	$\text{ng g}^{-1}$	590	29
Sm	$\text{ng g}^{-1}$	200	27
Eu	$\text{ng g}^{-1}$	73	9
Gd	$\text{ng g}^{-1}$	270	27
Tb	$\text{ng g}^{-1}$	53	25
Dy	$\text{ng g}^{-1}$	280	24
Ho	$\text{ng g}^{-1}$	71	23
Er	$\text{ng g}^{-1}$	210	22
Tm	$\text{ng g}^{-1}$	35	19
Yb	$\text{ng g}^{-1}$	200	17
Lu	$\text{ng g}^{-1}$	38	16
Hf	$\text{ng g}^{-1}$	160	16
W	$\text{ng g}^{-1}$	160	21
Re	$\text{ng g}^{-1}$	70	33
Ir	$\text{ng g}^{-1}$	840	13
Pt	$\mu\text{g g}^{-1}$	1.4	14
Th	$\text{ng g}^{-1}$	42	11
U	$\text{ng g}^{-1}$	11	13

chondrites are generally present at lower abundances and MIL 07273 is no exception (Fig. 2b, Mn-Zn). The data indicate that MIL 07273 is an ordinary chondrite, and siderophile element abundances are consistent with the H chondrite group.

### Physical Properties

During chipping and grinding for elemental analysis, we observed that MIL 07273 is exceptionally hard and coherent. Microtomography data were used to determine physical properties of MIL bulk samples, including volume, porosity, metal and sulfide content and shapes, and bulk density. Two-dimensional tomography image “slices” show metal, silicate, and voids within the sample, and 3-D data were used to reconstruct the shapes of metal grains (Fig. 3). The sample mass-weighted mean bulk density of MIL 07273 determined by  $\mu\text{CT}$  analysis is  $3.52 \pm 0.09 \text{ g cm}^{-3}$  (see Table S1 in supporting information), which is slightly higher than the mean H chondrite bulk density of  $3.42 \pm 0.18 \text{ g cm}^{-3}$  (Consolmagno et al. 2008). L and LL ordinary chondrites possess even lower bulk densities because of their lower reduced metal content. The bulk density of MIL is most akin to the H chondrites.

The slightly elevated bulk density of MIL 07273 compared to H chondrites may be explained in part by the unusually low porosity of the sample,  $0.6 \pm 0.2\%$  (Table S1). In comparison, H chondrites have an average mean porosity of 7.0% (Consolmagno et al. 2008). Microcrack porosity, generally easily visible in  $2.6 \mu\text{m}/\text{voxel}$  resolution volumes (see Friedrich and Rivers 2013), is nearly absent in MIL 07273. Another indication of a relative lack of microcracks is that the porosity values at two resolutions are nearly identical. If significant microcracks were present, one would expect a higher porosity at a higher resolution. Thus, MIL has atypically low porosity and microcracking. However, MIL 07273 does have some coarser intergranular porosity (Fig. 3a) and does have ultra-fine-scale microcracks visible in thin section.

The shape preferred orientation of metal grains in a sample can be used to quantitatively examine the degree of impact-related compaction the sample has experienced (Friedrich et al. 2008, 2014, 2017). The preferred orientation is measured by a strength factor, designated C (Woodcock 1977; Woodcock and Naylor 1983), which represents the degree of alignment of the long axes of metal grains. This value increases as metal grains rotate, align, and deform during impact compaction (Friedrich et al. 2008, 2014). The value of C for MIL is  $0.25 \pm 0.04$  (Table S1), which is moderately

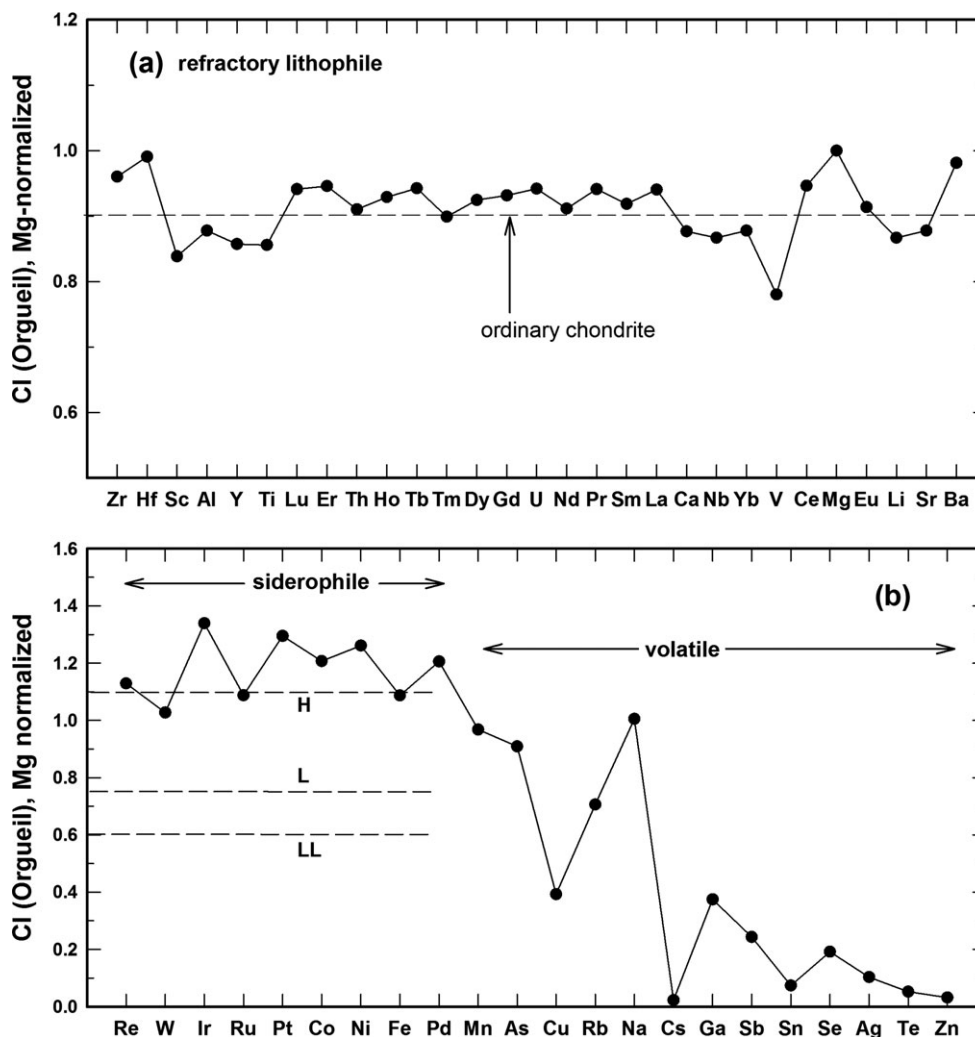


Fig. 2. CI-chondrite and Mg normalized abundances of 51 major, minor, and trace elements in MIL 07273, including (a) refractory lithophile elements, and (b) siderophile and volatile elements, arranged in order of increasing putative volatility (left to right). Orgueil normalization was done with trace element data from Friedrich et al. (2002) and major element Orgueil data from Anders and Grevesse (1989). Approximate H, L, and LL chondrite siderophile levels are from Kallemeyn et al. (1989).

low given the shock stage (discussed in the following section).

In terms of both low porosity and low value of  $C$ , among ordinary chondrites MIL most closely resembles Portales Valley, an H chondrite metallic melt breccia (Fig. 4; Friedrich et al. 2017). However, MIL 07273 differs sharply from Portales Valley in having a much higher shock stage (S4 versus S1, respectively), as described in the following section.

### Metal and Troilite Abundance

Estimates of metal and troilite contents for MIL were obtained in thin section using different data sets, as well as in bulk samples using  $\mu$ CT data. Results are shown in Table 3. Thin section estimates indicate ~8–10

area% metal and ~2.5–3.6 area% troilite, and  $\mu$ CT data average ~7.6 vol% metal ( $7.1 \pm 1.2\%$  metal mass-weighted average, Table S1) and ~1.4 vol% troilite (Table 3). This compares to an estimated  $7.3 \pm 0.7$  vol% Fe metal and  $4.0 \pm 0.3$  vol% troilite for average H chondrites, assuming reasonable densities for Fe-Ni metal and troilite in ordinary chondrites ( $7.5 \text{ g cm}^{-3}$  and  $4.6 \text{ g cm}^{-3}$ , respectively), the mean bulk density of H chondrite falls ( $3.42 \text{ g cm}^{-3}$ ; Consolmagno et al. 2008), and the mean reduced Fe abundance (15.98 wt%) and mean S content of H chondrite fall given by Jarosewich (1990). The metal content of MIL 07273 is similar to average H chondrites, indicating an H chondrite affinity for the meteorite. The MIL troilite content is somewhat low compared with average H chondrites, especially for the  $\mu$ CT data sets.



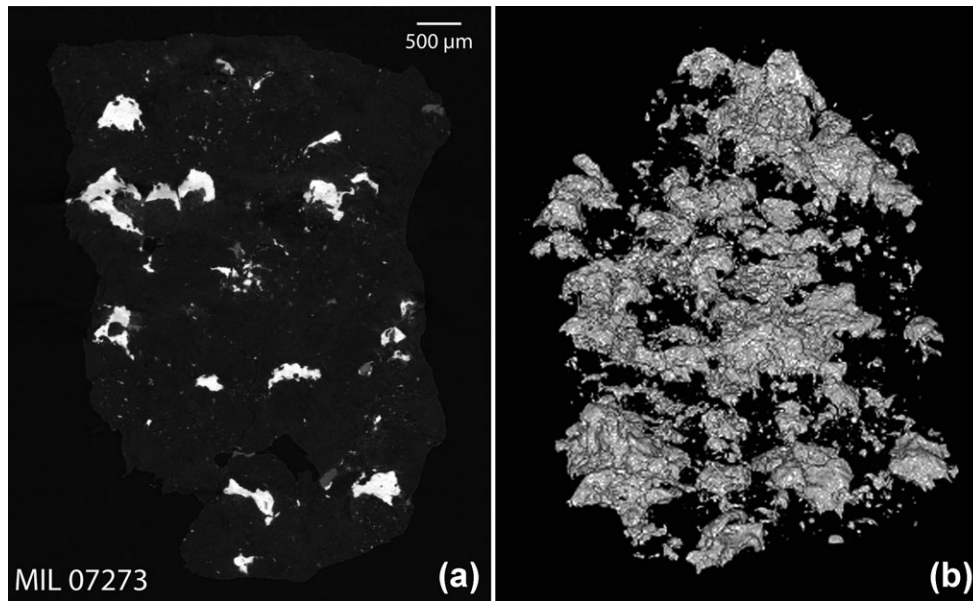


Fig. 3. Synchrotron X-ray microtomography data for MIL 07273 (subchip from MIL 07273,10). a) Typical X-ray microtomography “slice” showing asymmetric metal grains (bright, convex upwards), silicates (medium gray), and some isolated, large, intergranular voids (black). b) 3-D visualization of metal grains, again showing metal shape asymmetry (convex upwards).

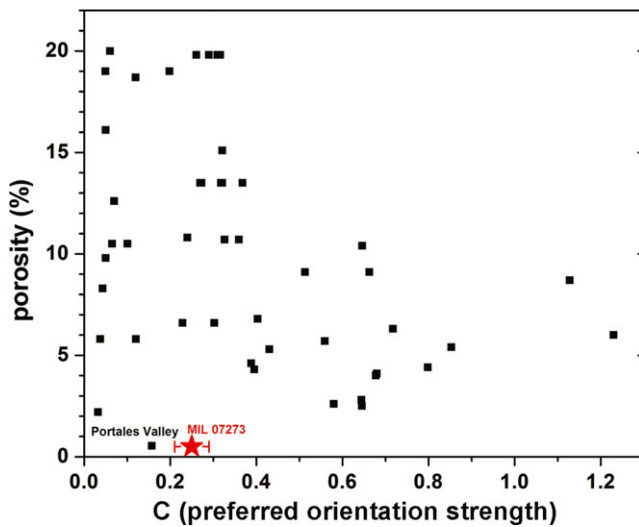


Fig. 4. Relationship between porosity and metal grain orientation strength factor C in MIL 07273 (this work) compared with other ordinary chondrites (Friedrich et al. 2008, 2013, 2017). Error shown for the C value in MIL is based on the five largest samples (Table S1). (Color figure can be viewed at [wileyonlinelibrary.com](http://wileyonlinelibrary.com).)

**Petrography**

In thin section, chondrules in MIL 07273 show evidence for fragmentation, and lithic and mineral clasts derived from chondrules range from clearly recognizable partial chondrules down to matrix grain (<5 μm) sizes

Table 3. Metal content in MIL 07273 estimated in thin-section sample (,12) and in μCT bulk samples (,6 and ,10) compared with average H chondrites (see text).

Data type	Metal (area%)	Troilite (area%)	Metal+troilite (area%)
EMPA map	10.5 <sup>a</sup>	2.5	13.0
Reflected light OM map	8.0	3.6	11.6
BSE map	–	–	13.8
μCT data, average	7.6 <sup>b</sup>	1.4 <sup>b</sup>	8.9 <sup>b</sup>
Mean H chondrite	7.3 <sup>b</sup>	4.0 <sup>b</sup>	11.3 <sup>b</sup>

<sup>a</sup>Includes 8.0% low-Ni metal, 2.5% high-Ni metal.

<sup>b</sup>Volume%.

(Figs. 5b–d, 5i, and 5j). Apparent chondrule sizes were measured in microprobe X-ray maps. Including what appear to be the most intact whole chondrules only, the apparent diameter is  $170 \pm 70 \mu\text{m}$  ( $n = 21$ ). Although the sample size is small, this diameter most resembles H chondrites (Friedrich et al. 2015). The fragmented nature of the chondrules hinders the size analysis measurements and likely biases the observed chondrule sizes to smaller values. Silicates in chondrules and chondrule fragments are “blackened” in transmitted light due to extensive cross-cutting by troilite-rich veins (Figs. 5b–j) (see discussion of veins in next section).

The matrix of the rock is almost entirely crystalline, with interlocking mineral grains. It is composed of fine-grained (apparent grain size <5 μm) silicates and small

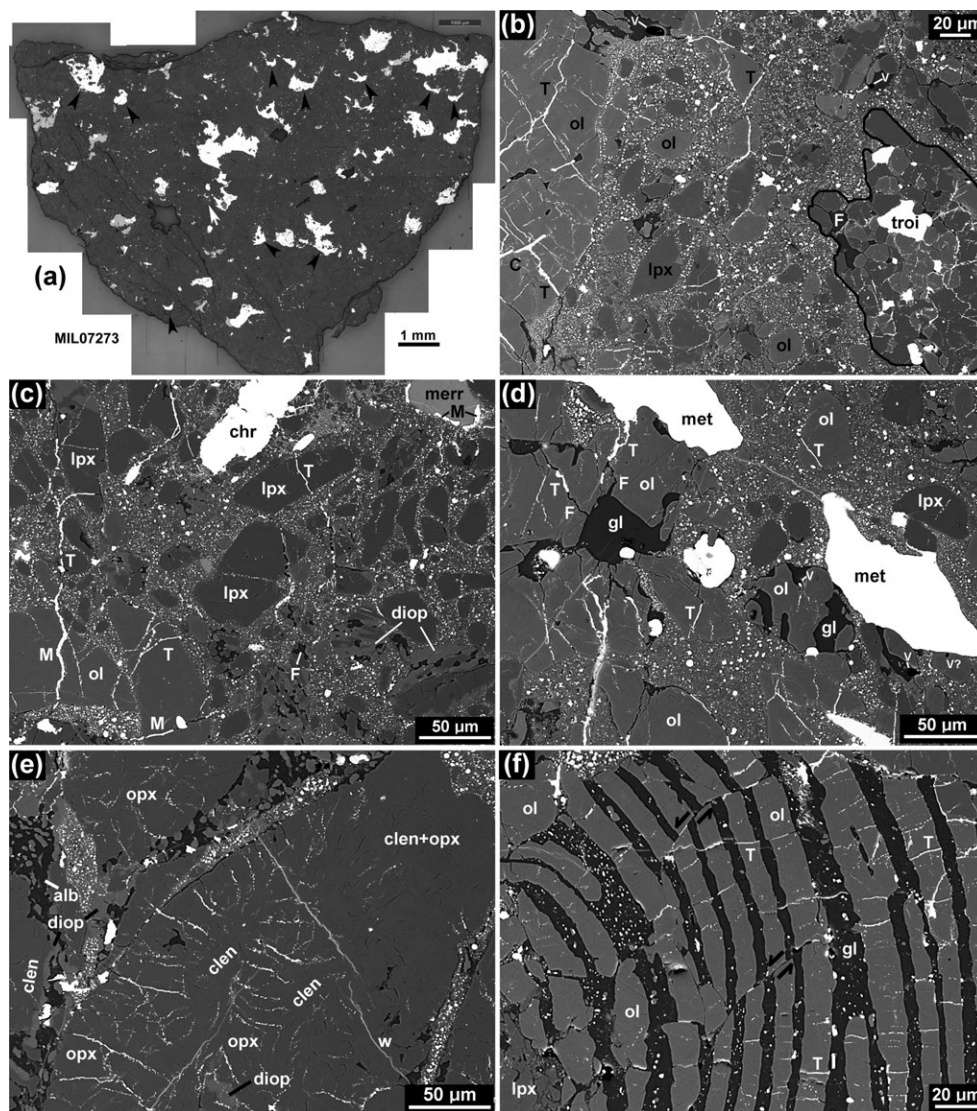


Fig. 5. Reflected light (a) and BSE images (b–l) of MIL 07273. Small bright spots in matrix areas (parts b–j) are mainly rounded metal grains. Phase abbreviations: ol = olivine; lpx = low-Ca pyroxene; opx = orthopyroxene; clen = clinoenstatite; troi or T = troilite, met or M = metal; ma = martensite; tae = taenite; merr = merrillite; F = feldspathic; alb = albitic feldspar; gl = feldspathic glass; chr or C = chromite; w = weathering product (Fe-hydroxides). a) Black arrows point to convex surfaces of asymmetric metal grains (white); a single white arrow (left center) points to the convex surface of a barred olivine chondrule with bent bars (shown in part f, arrow sense pointing from right to left in that figure). b) Melt matrix area with small clasts between larger veined clasts at left and at right (outlined). At left, a chromite vein (C) in olivine is cross-cut and displaced by a troilite vein. In the clast at right, troilite veins surround individual grains of olivine and low-Ca pyroxene. c) Melt matrix area with a variety of mineral and lithic clasts, including fragments of merrillite (upper right) and what are likely fragments of chondrule mesostases (bottom right) that contain diopsidic pyroxene and feldspathic material (dark gray). d) Area containing glass in chondrule fragments. e) Area (site 232) rich in coarse low-Ca pyroxene that contains an intergrowth of mostly vein-free clinoenstatite and veined orthopyroxene. Interclast areas between coarse pyroxene contain vein-free albitic feldspar + diopside (apparent chondrule mesostases) or metal-rich melt zones. f) Barred olivine chondrule clast (site 226) containing deformed olivine bars, including microfaults (half arrows show sense of displacement). g) Close-up of melt matrix in site 257, containing an orthopyroxene clast with magnesian overgrowth, and a metal-troilite globule. h) Close-up of melt matrix, containing many small olivine clasts. i) Close-up of melt matrix containing a glass patch with a prominent vesicle (V). j) Clast in site 257 that contains crystalline feldspar (albite-oligoclase), merrillite, chromite, and troilite at edge of melt matrix area (lower right). k) Coarse metal appears to fill interstices between silicates, has many inclusions, and is in contact with coarse merrillite. l) Ni-rich metal particle; Ni X-ray map shown in inset. The latter shows a Ni-rich rim surrounding the entire particle as well as diffuse variations in Ni intensity, with high-Ni areas enclosing taenite (outlined in main image) but extending in diffuse bands away to upper left and upper right. Troilite at the periphery of the metal particle connects to troilite veins that extend away from the particle.



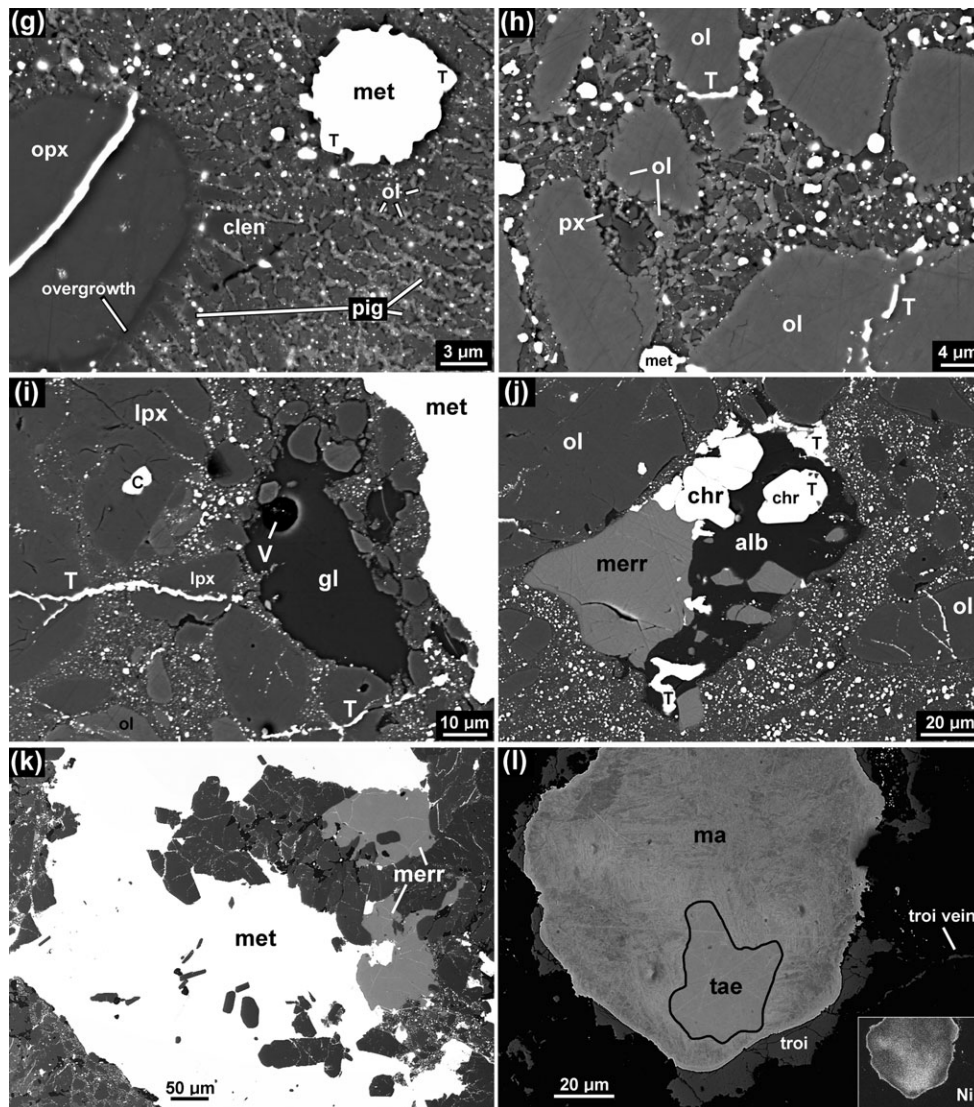


Fig. 5. Continued

(mainly <10 μm diameter) metal-troilite globules (Fig. 5g) and numerous small (≤1 μm) rounded metal blebs among silicates (Figs. 5g–j).

Metal is also present as a coarse (~100–1000 μm) fraction similar in size to chondrule clasts (Figs. 5a, 5d, 5k, and 5l). Coarse metal grains have scalloped edges, appearing to fill interstices of adjacent silicates, and commonly contain inclusions (Fig. 5k).

Three-dimensional examination by μCT scanning of MIL shows that the coarse metal grains have a distinctive asymmetric shape. These grains are vaguely cone-shaped, being convex on one side and more concave and irregular on the other (Fig. 3). Further, the cones are locally aligned (Fig. 3). Similar asymmetric shapes and alignment are evident (although biased by sectioning) in thin section (Fig. 5a).

We determined misorientation angles and other petrographic features for 44 olivine grains (≥50 μm) in chondrule clasts and used these data to assign shock stages to individual olivine grains following the procedure of Jamsja and Ruzicka (2010), after Stöffler et al. (1991), Schmitt and Stöffler (1995), and Schmitt (2000). As shown in Fig. 6, the deformation character of these olivine grains is notably unimodal. With 75% of the grains showing weak mosaic extinction, the data are consistent with a “conventional shock stage” (Stöffler et al. 1991) of S4 and a “weighted shock stage” (Jamsja and Ruzicka 2010; Ruzicka et al. 2015) of  $S4.0 \pm 0.5$ .

Examination of thin-section MIL 07273,12 in reflected light shows very minor replacement by iron oxides/hydroxides along metal grain boundaries, as well

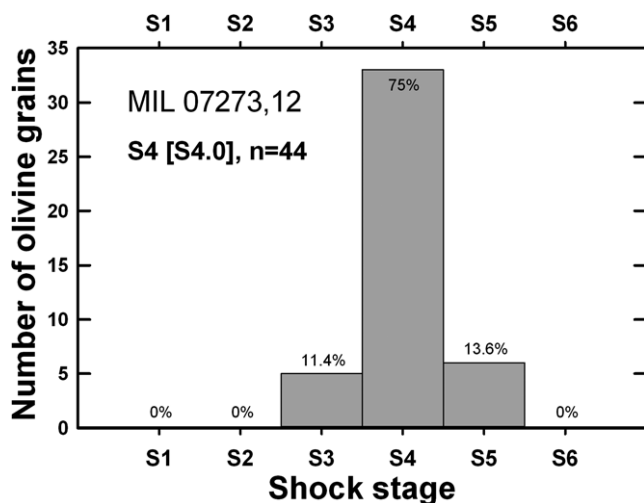


Fig. 6. Shock stages of olivine grains in MIL, together with the inferred overall conventional and weighted (in brackets) shock stage.  $n$  = total number of olivine grains.

as limited replacement by iron oxides/hydroxides of troilite in fine veins and metal in small metal/sulfide globules. Overall, less than 2% of the metal and sulfide in the thin section studied has been replaced by weathering product, indicative of a weathering grade of W1 (Wlotzka 1993). This is in contrast to the weathering grade of B/C originally reported for this stone (Weisberg et al. 2010).

### Mineralogy and Mineral Textures

Optical, SEM, and EBSD methods were used to study the mineralogy of matrix, clasts, and metal. Chondrule fragments are composed chiefly of olivine and low-Ca pyroxene (commonly orthopyroxene, with irregular patches of clinoenstatite) and contain mesostasis composed of high-Ca pyroxene and feldspathic material (mainly crystalline plagioclase feldspar, less commonly glass). Smaller clasts (<50–70  $\mu\text{m}$  across) consist of individual olivine and pyroxene grains and “mesostasis lumps” (clasts rich in feldspar and diopside, Fig. 5c). Other nonmatrix minerals observed are merrillite (with one single grain of Cl-apatite observed), chromite, troilite, and FeNi metal.

Troilite is found primarily in veins, less often as partial rims around coarser metal grains and matrix metal globules, and rarely as isolated compact grains (Figs. 5g, 5j, and 5l). Troilite-rich veins are typically  $\leq 3 \mu\text{m}$  wide and extend for tens to hundreds of microns. In places, the veins are discontinuous in the host mineral and form inclusion trails (Fig. 5h). Although dominantly composed of troilite, veins are locally composed of feldspathic material (Fig. 5d),

Fe-Ni metal (Fig. 5c), and rarely chromite (Fig. 5b), which alternate with the troilite or commonly with segments of open, fine-scale cracks. Veins never cross-cut metal. The veins cross clasts and are typically truncated at mineral and clast boundaries, but sometimes cross-cut both clasts and adjacent matrix, and show large variations in spatial density (Figs. 5b–e). Veins in chondrule clasts sometimes fill orthogonal or conjugate fractures (Fig. 5b), or are subparallel (Fig. 5e), or surround individual grains or clasts (Figs. 5b and 5c). In all areas studied with EBSD, troilite in veins that appears physically continuous or that is near other veins has a single crystallographic orientation, with no evidence of internal grain boundaries. These veins, thus, likely represent single grains with a sheet-, comb-, or net-like structure depending on whether parallel or intersecting vein sets are present.

Veining is most extensive in coarser olivine; common in low-Ca pyroxene (orthopyroxene) and larger chromite grains; relatively infrequent in matrix; and uncommon in feldspar, feldspathic glass, high-Ca pyroxene, or merrillite. Barely visible inclusion trails are more common in feldspar, Ca pyroxene, and merrillite than continuous veins, which are almost absent in these minerals.

Although most pyroxene grains in chondrule clasts are heavily veined by troilite, in some clasts, this veined pyroxene is interrupted by regions of vein- and fracture-free pyroxene (Fig. 5e). Although chemically similar, EBSD data show that the veined pyroxene indexes as orthopyroxene (hypersthene), and that the vein-free pyroxene indexes as clinoenstatite with subordinate pigeonite (Fig. 5e). Cross-cutting relationships here imply secondary formation of clinoenstatite/pigeonite after orthopyroxene was veined. In an adjacent chondrule, clinoenstatite and pigeonite predominate over orthopyroxene in a chondrule that lacks veins.

Matrix areas are distinctly rich in pyroxene, poor in feldspar, and somewhat poor in olivine compared with the host chondrite (Figs. 5g and 5h). EBSD mapping indicates that the chief pyroxene phases in matrix are the clinoenstatite and pigeonite polytypes (space group  $P2_1/c$ ). In two areas well-studied with EBSD, these two pyroxenes comprise ~60–70% of the matrix (Table 4; Fig. 7). Given their similar structures and cell parameters, the two minerals are difficult to reliably distinguish with EBSD, but some grains index primarily as clinoenstatite and some as pigeonite, and both phases seem to be present given variations in composition. Both minerals form equant or slightly elongate, blocky subhedral grains typically  $\leq 1\text{--}4 \mu\text{m}$  across, or overgrowths on orthopyroxene (hypersthene) mineral clasts (Figs. 5g and 5h).



Table 4. Mineralogy of two matrix-rich areas in MIL 07273 derived from EBSD mapping. “Complete” includes all clasts and matrix in the entire area; “matrix” excludes larger (>20  $\mu\text{m}$ ) clasts and has phase proportions renormalized to 100%.

Step interval ( $\mu\text{m}$ )	Site 273 #2 <sup>a</sup>		Site 257 <sup>b</sup>	
	Complete	Matrix	Complete	Matrix
Area ( $\mu\text{m}^2$ )	13574	5477	84892	16653
Mode (pixel%)				
Olivine	20.2	10.2	34.3	17.2
Orthopyroxene	14.6	10.4	4.2	4.1
Clinoenstatite	16.2	20.8	20.6	45.8
Pigeonite	30.3	38.8	10.3	22.4
Diopside	6.3 <sup>c</sup>	8.1 <sup>c</sup>	0.98	1.6
Albite	1.3	1.6	4.3	3.1
Troilite	4.4	5.1	1.1	0.45
Bcc metal	0.64	0.83	2.4	4.4
(kamacite + martensite)				
Fcc metal (taenite)	1.8 <sup>c</sup>	2.6 <sup>c</sup>	0.05	0.04
Chromite	n.a. <sup>d</sup>	n.a. <sup>d</sup>	1.2	0.24
Merrillite	1.5	1.8	3.1	0.69
Zero solutions	2.4	–	17.5	–

<sup>a</sup>0.13  $\times$  0.1 mm map area; as-acquired data set, using Optimized EBSD indexing.

<sup>b</sup>0.34  $\times$  0.25 mm map area; reanalyzed data set, using Refined Accuracy indexing (regarded as more accurate than Optimized EBSD).

<sup>c</sup>Likely overestimate.

<sup>d</sup>Not analyzed.

Olivine typically occurs in the matrix as slightly irregular grains  $\leq 2 \mu\text{m}$  long and  $< 1 \mu\text{m}$  wide occupying interstices between matrix pyroxene grains (Figs. 5g and 5h). Chondrule-derived olivine mineral clasts in the matrix areas have thin epitaxial overgrowths that connect to elongate matrix olivine grains that extend away from the clasts (Fig. 5h).

The appearance of matrix olivine and pyroxene grains is variable. In some matrix areas, matrix pyroxene and olivine are aligned to form segmented chains with a vaguely dendritic texture (Fig. 5g). In other areas, grains appear more randomly oriented (Fig. 5h). EBSD data for matrix areas indicate that there are preferred crystallographic orientations of clusters of olivine and pyroxene grains forming localized domains, up to  $\sim 30$ – $40 \mu\text{m}$  across for pyroxene (Fig. 7) and up to  $\sim 20$ – $30 \mu\text{m}$  across for olivine.

Other phases are present in matrix areas as either small clasts or as “true” matrix phases (i.e., seemingly cogenetic with matrix pigeonite, clinoenstatite, and olivine). Orthopyroxene is present (Table 4), but most if not all of this orthopyroxene appear to represent small clasts (Figs. 5g, 7, and 8), based on deformation, as

discussed later. Small clasts of olivine are present (Figs. 5h, 7, and 8) and can be unambiguously identified as clasts owing to their different composition compared to matrix olivine. Other phases intrinsic to matrix include small amounts of Ca-rich pyroxene grains interstitial to olivine and low-Ca pyroxene, numerous metal globules or blebs composed mainly of bcc metal, and troilite surrounding metal (Fig. 5g) or present as veins (Figs. 5c, 5i, and 8).

Feldspathic material is also present in both matrix and clasts in a variety of forms. EBSD data confirm that much of this is crystalline feldspar (Figs. 5j and 7). Albitic feldspar is commonly found with diopside in discrete clasts or “mesostasis lumps” (Figs. 5c and 5e).

Glass occurs (1) within the mesostases of small clast (chondrule) fragments (Fig. 5d) and (2) as uncommon patches in matrix (Fig. 5i). Small amounts of glass may also locally occur interstitial to matrix silicates. Glass in clasts is sometimes surrounded by radiating cracks filled with feldspathic material or troilite, but itself is not fractured (Fig. 5d), in this way resembling maskelynite (Chen and El Goresy 2000). In contrast, glass patches in matrix lack radiating fractures and appear to grade into their surroundings, inter-fingering with matrix minerals (Fig. 5i). Both occurrences of glass can contain circular or elongate voids that could be vesicles (best seen in Fig. 5i), which is unlike maskelynite (Chen and El Goresy 2000). In addition to being observed in numerous glass patches, a single vesicle was found at the edge of one crystalline feldspar area.

Coarse FeNi metal in MIL 07273 is nearly featureless in optical and BSE images and lacks the plessite or coarse blocky intergrowths of kamacite and taenite/tetrataenite typically found in chondrites, or the dendritic metal-sulfide intergrowths typically found in rapidly cooled shock melts of chondrites. Metal is polycrystalline, as evidenced by faint internal grain boundaries in BSE images and by EBSD data that indicate grains of differing crystallographic orientation. Inclusions occur at internal metal grain boundaries and are composed of low-Ca pyroxene, troilite, chromite, merrillite, and feldspar, with both low-Ca pyroxene and chromite enclosed within metal sometimes being veined by troilite. Metal grain sizes within coarse particles appear to be  $\sim 10$ – $200 \mu\text{m}$  across. Coarse metal is often surrounded by grains of merrillite or troilite (Figs. 5k and 5l). Merrillite grains at the edges of coarse metal are up to  $\sim 0.5 \mu\text{m}$  across, but smaller grains also are present in clasts not in obvious contact with metal (Fig. 5j).

Metal is largely bcc (body-centered cubic) structured, including kamacite and martensite, but fcc (face-centered cubic) metal (taenite) is also present. Martensite has a faintly mottled appearance in optimized BSE images (Fig. 5l) and is less perfectly

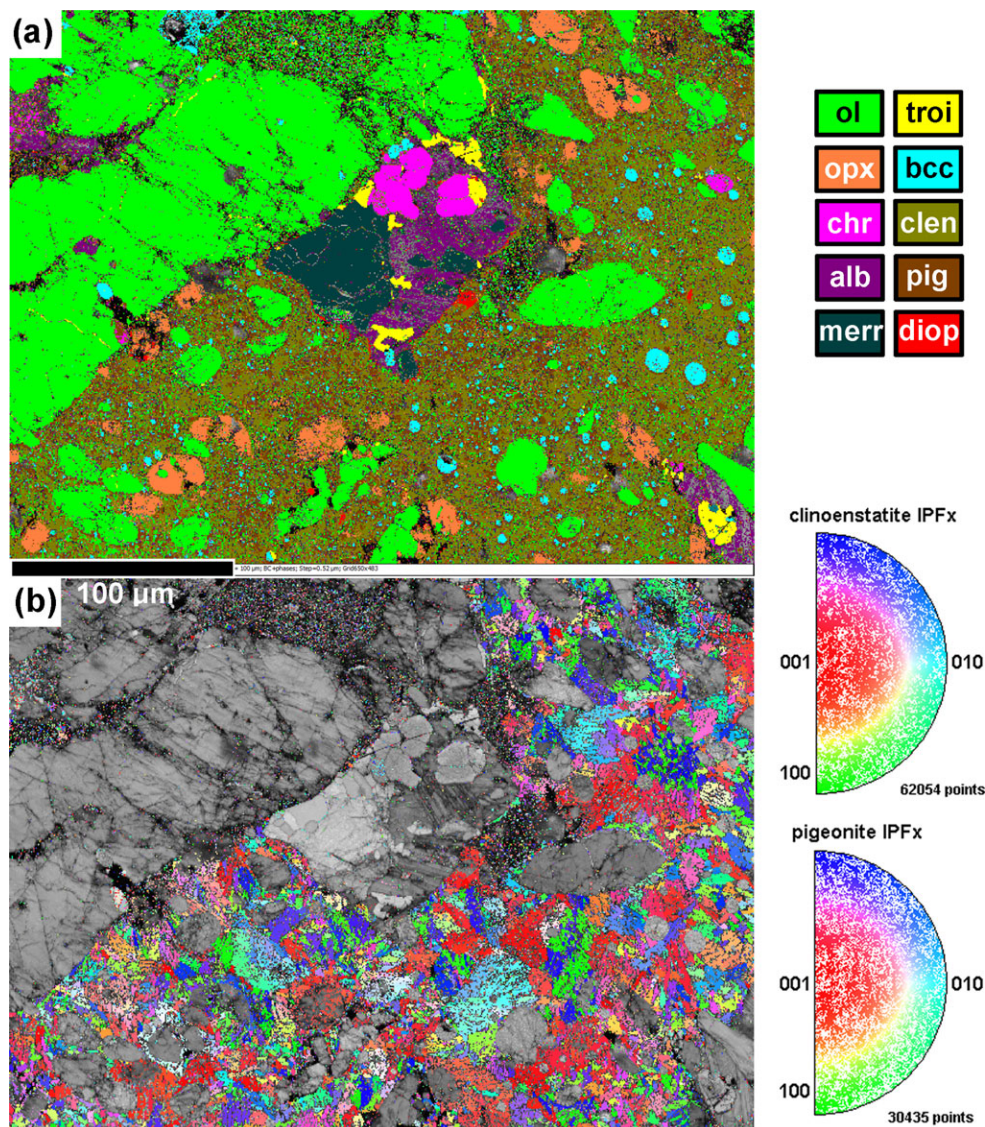


Fig. 7. EBSD data for site 257. Matrix containing small clasts extends over half of this image on the lower right; a small clast near center is shown with a BSE closeup in Fig. 5j. Scale bar = 100  $\mu\text{m}$ . a) Phase + band contrast map, with colors representing phases (ol = olivine = light green; opx = orthopyroxene = orange; chr = chromite = pink; alb = albite = dark purple; merr = merrillite = dark green; troi = troilite = yellow; bcc = bcc metal = light blue; clen = clinoenstatite = olive; pig = pigeonite = dark brown; diop = diopside = red). Matrix is rich in clinoenstatite and pigeonite. b) IPF<sub>x</sub> (inverse pole figure-x) + band contrast map, with colors representing crystallographic orientations of clinoenstatite and pigeonite grains relative to the x (right–left) direction (upper hemisphere folded inverse pole figures at right; red coloration indicates grains with  $\langle 001 \rangle$  oriented left–right, etc.). Matrix clinoenstatite and pigeonite form common crystallographic orientations over regions larger than their apparent grain sizes (part a), implying that grains connect in the third dimension. A color version of this figure is provided in electronic web versions of this article. (Color figure can be viewed at [wileyonlinelibrary.com](http://wileyonlinelibrary.com).)

crystalline than either kamacite or taenite, being darker in EBSD band contrast images (Fig. 9c). The taenite in Fig. 9 is composed of three grains that form a cluster, with smooth or straight boundaries between the grains internal to the cluster, and with an irregular outline for the overall shape of the cluster. Taenite grains in other metal particles also have irregular exterior shapes (Fig. 5l).

No unambiguous high-pressure polymorphs were found in matrix or elsewhere; instead MIL has a low-pressure mineralogy.

### Mineral Deformation

The deformation of various minerals in MIL 07273 was studied by EBSD techniques. Plastic deformation



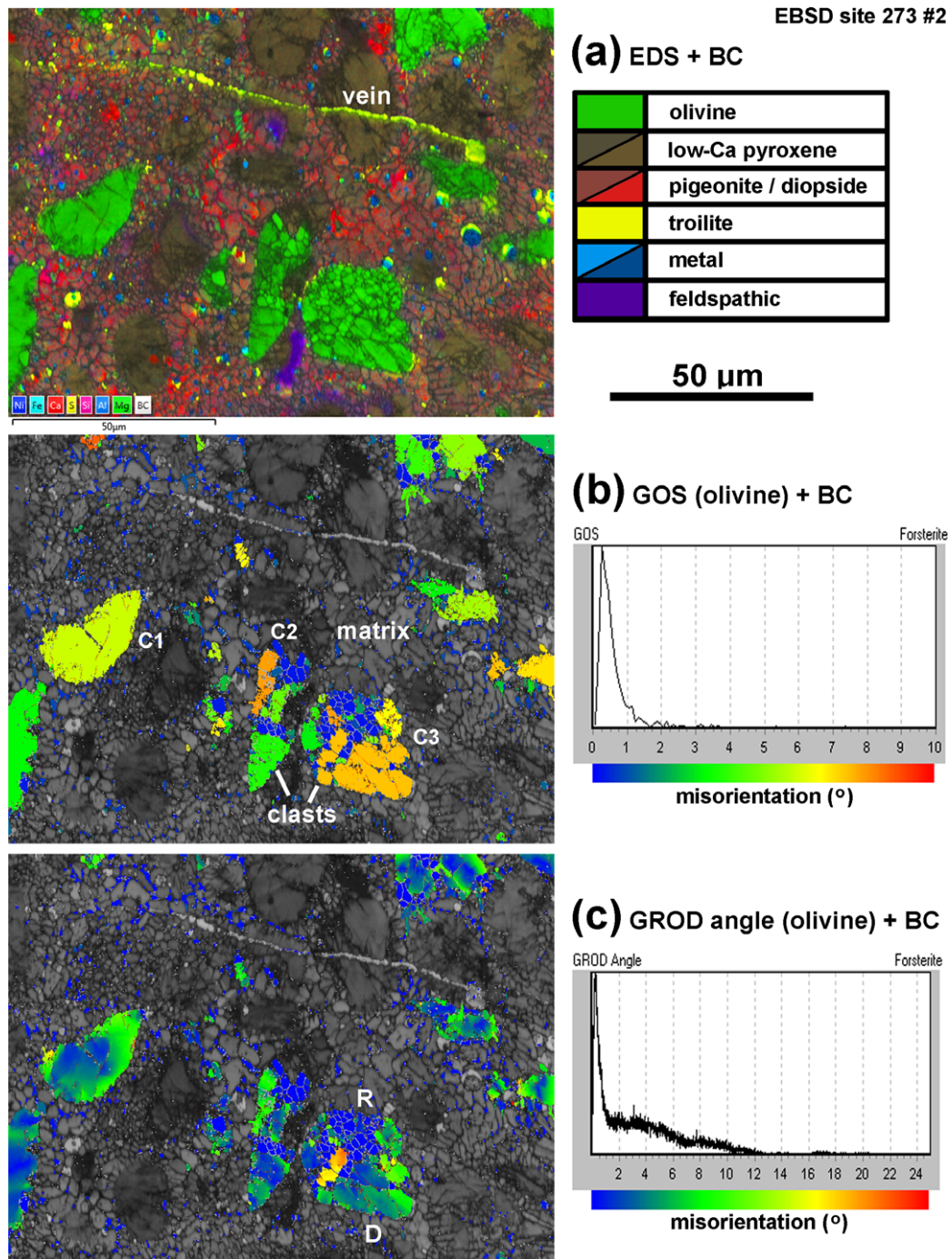


Fig. 8. EBSD and chemical data for matrix site 273 #2. Scale bar = 50  $\mu$ m. a) EDS (energy dispersive spectrometer) chemistry + BC (band contrast) map. Colors correspond to compositions and different phases as given in the legend. A troilite vein cross-cuts both matrix and clasts at top. b) GOS + BC map. Colors represent GOS values (in degrees) in olivine and are a measure of average angular misorientation within grains. Most matrix olivine (tiny interstitial) grains have low values of GOS ( $<1^{\circ}$ , blue), whereas clasts typically have higher values (1–8 $^{\circ}$ , green to orange) except where recrystallized (blue). Clast 1 (C1) is deformed but not recrystallized, whereas clasts 2 (C2) and 3 (C3) are partly recrystallized. c) GROD (grain reference orientation deviation) angle + BC image. Colors show GROD angle values (in degrees) in olivine, which visualizes the distortion of crystal lattice from a reference value (average orientation) for the grain. Matrix olivines and recrystallized portions of grains have low GROD angle values ( $<1^{\circ}$ , blue), whereas clasts are more distorted (1–17 $^{\circ}$ , blue-green to orange), with greater distortion often at their edges (e.g., clast C1). Recrystallized (R) and deformed (D) portions of clast C3 are identified. A color version of this figure is provided in electronic web versions of this article. (Color figure can be viewed at [wileyonlinelibrary.com](http://wileyonlinelibrary.com).)



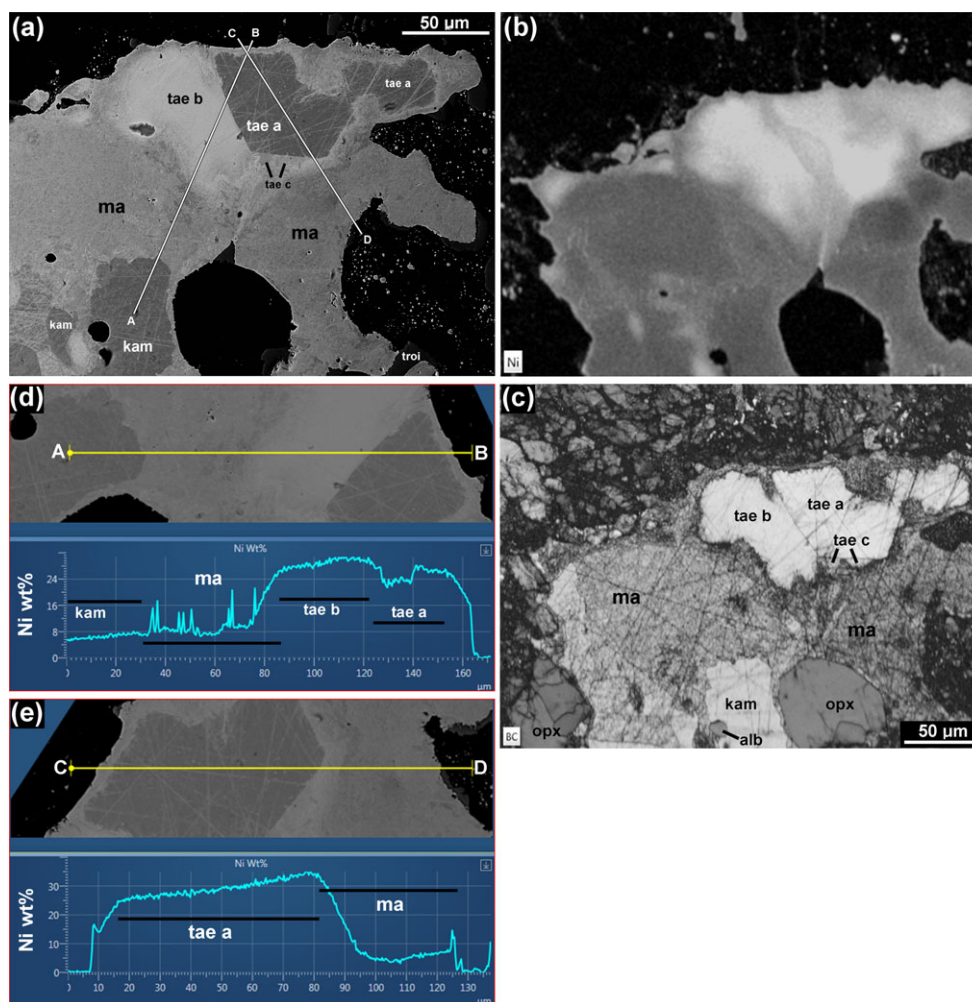


Fig. 9. Data for coarse FeNi metal, site 251. Mineral abbreviations: tae = taenite (tae a, b, c identify different grains), kam = kamacite, ma = martensite, opx = orthopyroxene, alb = albitic feldspar, troi = troilite. a) Backscattered electron image showing traverse 1 (A–B) and 4 (C–D) locations. b) Ni X-ray map. Martensite surrounding taenite (upper right) is enriched in Ni, forming a diffuse halo. c) EBSD band contrast image, with brightness related to crystallinity (brighter = stronger diffraction bands, darker = weaker). Martensite has weaker band contrast than kamacite and taenite, especially close to taenite in the Ni-rich halo. d) Traverse 1 Ni concentration profile. e) Traverse 4 Ni concentration profile. A color version of this figure is provided in electronic web versions of this article. (Color figure can be viewed at [wileyonlinelibrary.com](http://wileyonlinelibrary.com).)

can be quantified by grain orientation spread (GOS), which gives the average angular misorientation within a grain (Brewer et al. 2009). Data show systematic differences in GOS values between minerals and differences between minerals in clasts and matrix. Troilite is among the least deformed minerals, with GOS values for grains mainly  $<1^\circ$ . Olivine and orthopyroxene grains in clasts tend to have the highest GOS values, often  $\sim 1\text{--}8^\circ$  but up to  $20^\circ$  for olivine, and often  $\sim 1\text{--}5^\circ$  but up to  $\sim 10^\circ$  for orthopyroxene. In contrast, matrix olivine, pigeonite, and clinoenstatite grains have typical GOS values of  $<1^\circ$ , with many grains having only  $\sim 0.3^\circ$ , which is close to the inferred detection limit. Matrix grains are unambiguously less

deformed than coexisting small clasts of olivine and orthopyroxene (Fig. 8). In places, olivine grains in these small clasts appear to have recrystallized, forming new, weakly deformed subgrains (Fig. 8). Albitic feldspar (oligoclase-albite), diopside, clinoenstatite, and pigeonite in chondrule clasts have moderate GOS values, mainly  $\sim 0.5\text{--}3^\circ$ , less than for coexisting olivine and orthopyroxene. Based on limited data, metal appears to have heterogeneous strain, with higher GOS values in what is interpreted as martensite ( $\sim 1\text{--}7^\circ$ ) than in kamacite and taenite ( $<1^\circ$ ). In one small clast (Fig. 5j), merrillite appears to have partly recrystallized, forming subgrains with GOS  $\sim 0.5^\circ$  adjacent to more deformed grains with GOS up to  $\sim 7^\circ$ .

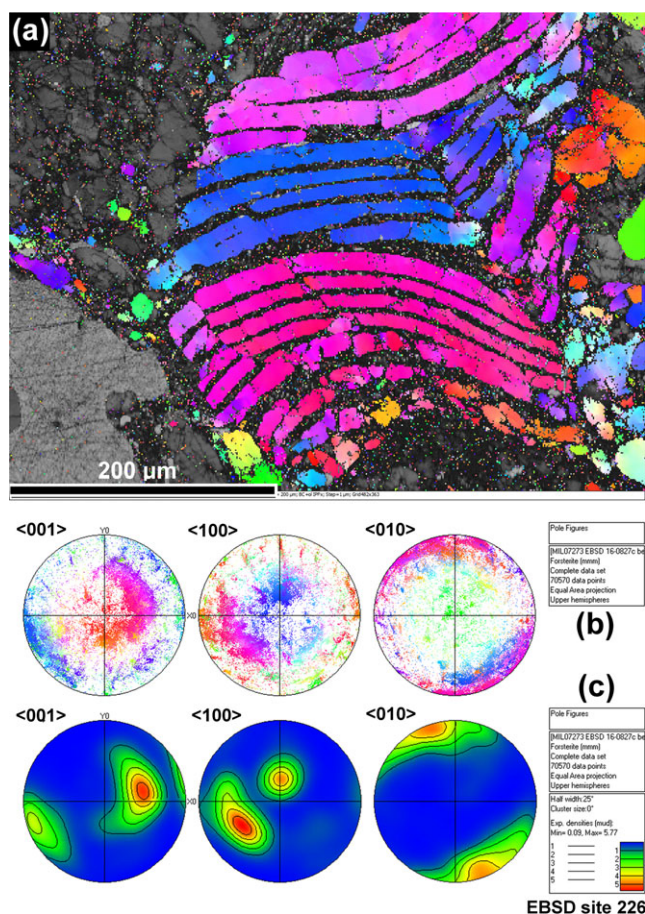


Fig. 10. EBSD data for site 226, which includes a deformed barred olivine chondrule clast. a) IPFz (inverse pole figure-z) + band contrast map, with colors related to crystallographic pole figures of olivine relative to the “z” or out-of-plane up direction. Figure is rotated 90° counter-clockwise relative to Fig. 5f, which includes a portion of this area. Scalebar = 200  $\mu\text{m}$ . b) Pole figure plot (upper hemisphere) showing olivine crystal orientation, with colors the same as in part (a). Most olivine grains have  $\langle 010 \rangle$  poles oriented close to the plane of the section in the upper left–lower right direction. c) Same as (b), except contoured by density of pole orientations in terms of multiples of uniform density (m.u.d., red-orange represents high values, blue represents low values; 25° half-width was assumed for contouring). This shows the common  $\langle 010 \rangle$  orientations for olivine but also the separation into two major groups of  $\langle 001 \rangle$  and  $\langle 100 \rangle$  orientations, implying rotation during deformation around the  $\langle 010 \rangle$  axis to form the two major orientations. A color version of this figure is provided in electronic web versions of this article. (Color figure can be viewed at [wileyonlinelibrary.com](http://wileyonlinelibrary.com).)

The highest GOS values for olivine (up to 20°) were found in an olivine clast that has curved olivine bars (Figs. 5f and 10). The olivine bars are cross-cut by troilite veins that do not continue into inter-bar mesostasis areas, which are largely feldspathic and glassy (Fig. 5f). Evidently, plastic deformation bent the

bars and brittle deformation created microfaults that locally displaced individual bars (Fig. 5f). Small amounts of troilite are present along some of the microfaults. EBSD data show that olivine in the bars has a generally common  $\langle 010 \rangle$  direction, with portions that significantly differ in their  $\langle 001 \rangle$  and  $\langle 100 \rangle$  orientations (Fig. 10). These data can be explained by derivation of the clast from a barred olivine chondrule that had one olivine crystal orientation prior to deformation, with olivine primarily rotating around its  $\langle 010 \rangle$  axis during deformation.

Although GOS values for individual olivine grains in the areas studied with EBSD can range to high values, most grains have lower values. The average values of GOS for olivine in five EBSD map sites are given in Table S3 in supporting information. Data are for grains  $>5 \mu\text{m}$  across (grain diameter of circle with equivalent area to measured grain) so as to exclude matrix grains. Mean GOS values for olivine in these sites range from 3.8 to 5.5° and are mainly  $\sim 4\text{--}5^\circ$ . A straight average of the five sites gives  $4.6 \pm 0.7^\circ$  (mean and standard deviation), and an average by olivine area gives  $4.1 \pm 2.3^\circ$ . The grain sizes of these grains are generally smaller than grains studied optically to determine shock stage. However, if the grains in both data sets are representative of the overall population of grains, it suggests that a weighted shock stage of S4.0 corresponds to an average olivine grain misorientation of  $\sim 4\text{--}5^\circ$ .

### Phase Chemistry

Phase chemistry data are given in Table 5 and are shown in Figs. 9 and 11–14. For average compositions of coarse olivine and low-Ca pyroxene in chondrule clasts, EMPA and SEM data agree within errors for all elements (Table 5). Although preliminary data were interpreted to indicate that MIL 07273 was a low-FeO chondrite similar to H but containing more magnesian olivine and low-Ca pyroxene (Weisberg et al. 2010), our data do not generally support this assessment. For coarse phases in MIL chondrule clasts, olivine Fa ( $16.9 \pm 0.6$ , mean and standard deviation of combined EMPA and SEM data) and orthopyroxene Fs values ( $15.7 \pm 1.0$ ) fall within the range for H4–6 chondrites (Fig. 11). The compositions are skewed to the lower range of normal H chondrite Fa and Fs values (Fig. 11). Coarse olivine and low-Ca pyroxene are highly equilibrated, with pyroxene Fs slightly more variable than olivine Fa, most consistent with type 5 metamorphic grade. A type 5 designation for chondrule clasts agrees with the preliminary classification of MIL 07273 (Weisberg et al. 2010).

Table 5. Average composition of phases in MIL 07273 determined with SEM (EDS mapping) and EMPA (WDS spot) methods.

Method	Olivine EMPA	Olivine SEM	Melt matrix olivine		Low-Ca pyroxene EMPA	Low-Ca pyroxene <sup>a</sup> SEM	Melt matrix pyroxene <sup>a</sup>		Diopside SEM	Feldspar SEM	Glass SEM	Chromite SEM	Merrillite SEM	FeNi metal <sup>b</sup> SEM
			SEM	SEM			SEM	SEM						
n	53	67	9	23	44	15	23	29	30	13	23			
Wt%														
SiO <sub>2</sub>	39.8 (0.3)	39.3 (0.7)	42.5 (3.3)	56.5 (0.8)	56.3 (0.7)	56.3 (1.9)	54.4 (1.4)	65.3 (1.5)	64.6 (1.2)	<0.4	<0.4	<0.4	—	
TiO <sub>2</sub>	<0.04	<0.4	<0.8	0.19 (0.07)	<0.3	<0.4	0.5 (0.3)	<0.4	<0.3	1.6 (0.5)	<0.4	<0.4	—	
Al <sub>2</sub> O <sub>3</sub>	<0.19	<0.3	3.5 (1.3)	0.21 (0.18)	<0.5	5.8 (1.9)	1.0 (0.7)	21.0 (0.6)	19.7 (1.1)	5.2 (0.3)	<0.2	<0.2	—	
Cr <sub>2</sub> O <sub>3</sub>	<0.04	<0.5	<1.2	0.30 (0.37)	<0.5	<0.5	1.0 (0.6)	<0.6	<0.7	59.8 (0.7)	<0.5	<0.5	—	
V <sub>2</sub> O <sub>5</sub>	n.a.	n.d.	n.d.	n.a.	n.d.	n.d.	n.d.	n.d.	n.d.	0.7 (0.5)	n.d.	n.d.	—	
FeO	16.1 (0.5)	15.9 (0.7)	17.6 (3.2)	10.8 (0.9)	10.4 (0.6)	8.1 (1.6)	3.8 (0.8)	<0.9	1.5 (0.5)	27.5 (1.6)	0.9 (0.3)	<0.3	—	
MnO	0.50 (0.02)	0.5 (0.3)	<1.3	0.56 (0.03)	0.5 (0.4)	<0.7	<0.4	<0.5	<0.4	0.7 (0.3)	<0.3	<0.3	—	
MgO	44.7 (0.4)	43.5 (0.7)	32.5 (2.9)	31.7 (0.5)	31.1 (0.7)	23.0 (3.2)	16.8 (0.5)	<0.4	1.1 (0.9)	4.0 (0.7)	3.5 (0.2)	<0.2	—	
CaO	0.03 (0.03)	<0.2	0.6 (0.5)	0.77 (0.10)	0.7 (0.3)	3.9 (1.9)	21.5 (1.6)	2.5 (0.6)	1.2 (0.8)	<0.4	46.3 (0.6)	<0.2	—	
Na <sub>2</sub> O	<0.05	<0.2	0.8 (0.6)	0.04 (0.03)	<0.2	2.3 (0.8)	0.7 (0.2)	9.3 (0.4)	8.6 (0.7)	<0.2	2.3 (0.2)	<0.2	—	
K <sub>2</sub> O	<0.02	<0.3	<0.4	n.d.	<0.2	0.3 (0.2)	<0.3	0.6 (0.3)	2.8 (0.3)	<0.2	<0.2	<0.2	—	
P <sub>2</sub> O <sub>5</sub>	n.a.	<0.4	<0.6	n.a.	<0.5	<0.9	<0.3	<0.6	<0.4	n.d.	45.4 (0.5)	<0.2	—	
Fe	—	—	—	—	—	—	—	—	—	—	—	—	91.0	
Ni	0.03 (0.03)	n.d.	n.d.	0.05 (0.05)	n.d.	<0.4	<0.3	<0.5	<0.4	n.d.	<0.4	<0.4	9.3	
S	n.a.	n.d.	<1.1	n.a.	n.d.	<0.3	<0.2	<0.2	<0.2	n.d.	<0.2	<0.2	—	
Total	101.1	99.2	99.7	101.2	99.0	100.6	99.9	98.7	99.5	99.5	98.4	98.4	100.3	
Mol%														
Fa	16.8 (0.5)	17.0 (0.7)	23.2 (3.2)											
Wo				1.4 (0.2)	1.4 (0.5)	9.4 (5.0)	44.8 (2.8)							
Fs				15.8 (1.3)	15.6 (0.8)	15.0 (2.0)	6.3 (1.3)							
En				82.7 (1.2)	83.0 (0.8)	75.6 (4.5)	48.9 (1.8)							
Ab								84.2 (2.5)	77.3 (4.2)					
Or								3.3 (1.6)	16.5 (1.6)					
An								12.4 (2.5)	6.2 (4.4)					

<sup>a</sup>Excludes Mg-rich overgrowths of clasts in melt matrix.<sup>b</sup>Area-weighted average, determined using a semi-automated, principal components, chemical grouping technique (Analyze Phases of AZtec 3.1), based on 1,758,856 classified metal pixels in 11 fields.

n = number of analyses. Values in parentheses are standard deviations. n.d. = not detected, n.a. = not analyzed, — = no value.



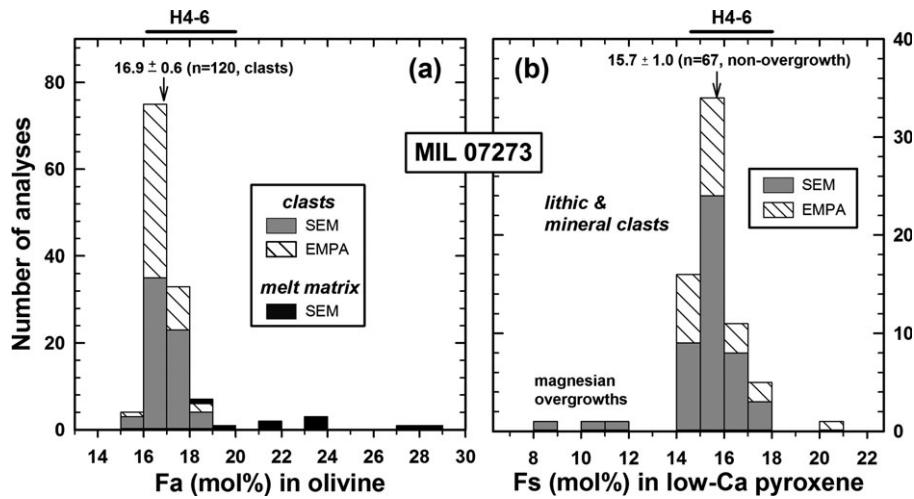


Fig. 11. Distribution of (a) olivine Fa and (b) low-Ca pyroxene Fs values in MIL 07273 compared to H4-6 chondrites (H4-6 range from Brearley and Jones 1998).

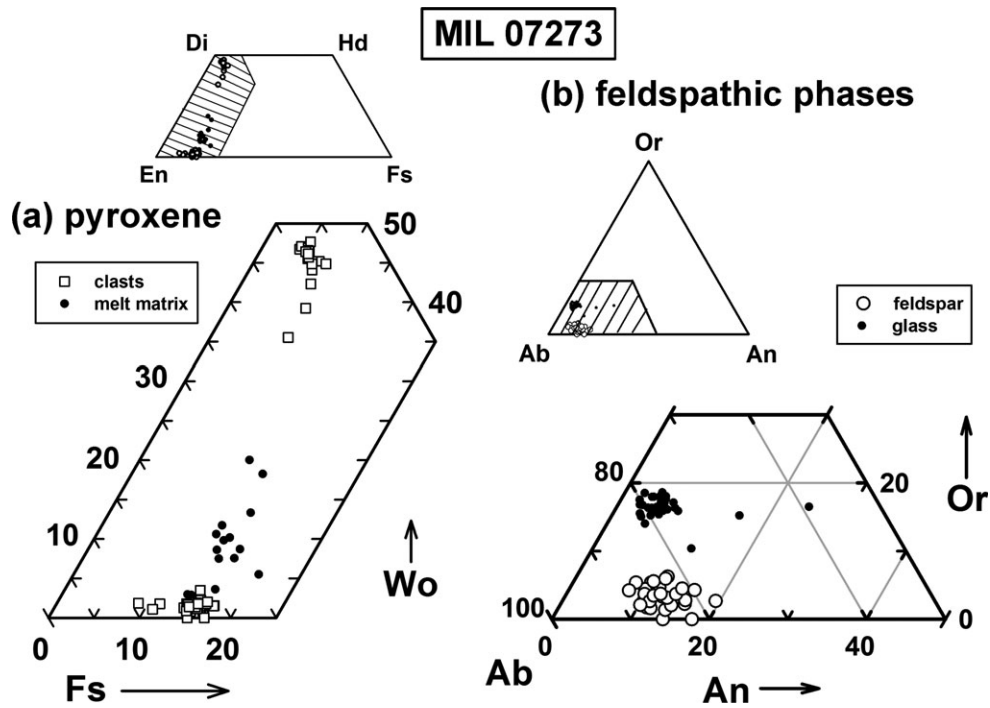


Fig. 12. Composition in MIL 07273 of (a) pyroxene minerals shown in the pyroxene quadrilateral and of (b) feldspathic phases shown in a portion of the feldspar ternary diagram, based on SEM data.

Other aspects of mineral compositions in MIL also resemble what is found in type 4-6 ordinary chondrites, and specifically in H4-6 chondrites. For example, MIL has an inferred average Ni content in metal of ~9.3 wt% (Table 5), which is similar to the value of ~9.8 wt% Ni for average H chondrite metal calculated from the H chondrite fall data of Jarosewich (1990). This Ni content

is significantly less than for bulk metal in L (~15.0 wt%) and LL (~30.5 wt%) chondrites (Jarosewich 1990). Comparing the major and minor element data for coarse phases (nonmatrix) in MIL (Table 5) to that compiled by Brearley and Jones (1998) for ordinary chondrites, the compositions of olivine, low-Ca pyroxene, diopside, merrillite, and chromite are all

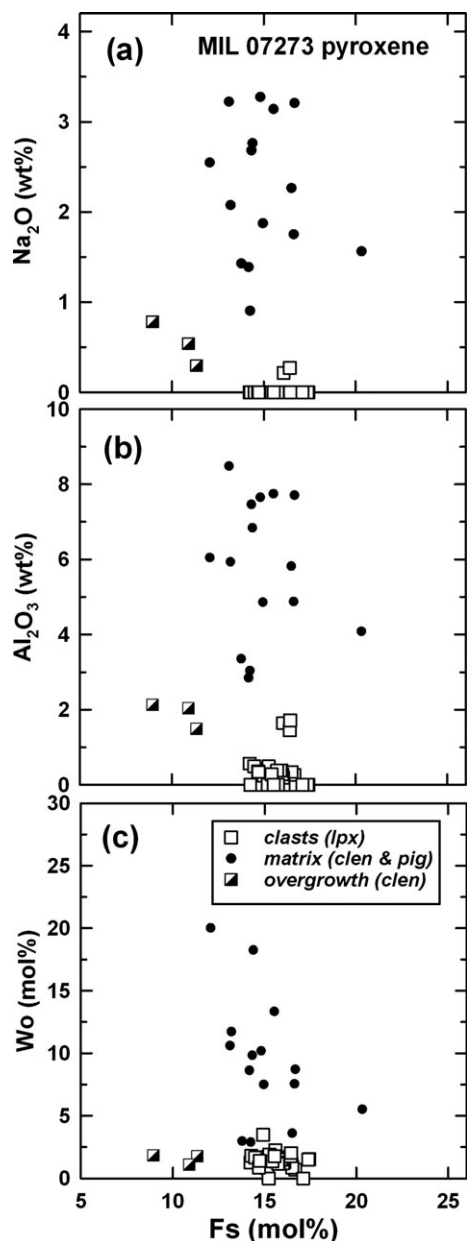


Fig. 13. (a) Soda, (b) alumina, and (c) Wo contents in relation to Fs values for pyroxene in MIL 07273, based on SEM data. lpx = low-Ca pyroxene, mainly orthopyroxene; clen = clinoenstatite; pig = pigeonite.

similar. In MIL 07273, feldspathic glass has higher Or and lower An content than feldspar (Fig. 12, Table 5). The compositions of these feldspathic phases bracket the Ab/Or/An values found in ordinary chondrites (Brearley and Jones 1998).

One striking difference between MIL and equilibrated ordinary chondrites is the presence of abundant matrix pigeonite and clinoenstatite in MIL. Pigeonite has variable Ca content, with a typical Wo value of ~10 mol% (Fig. 12). Overgrowths of

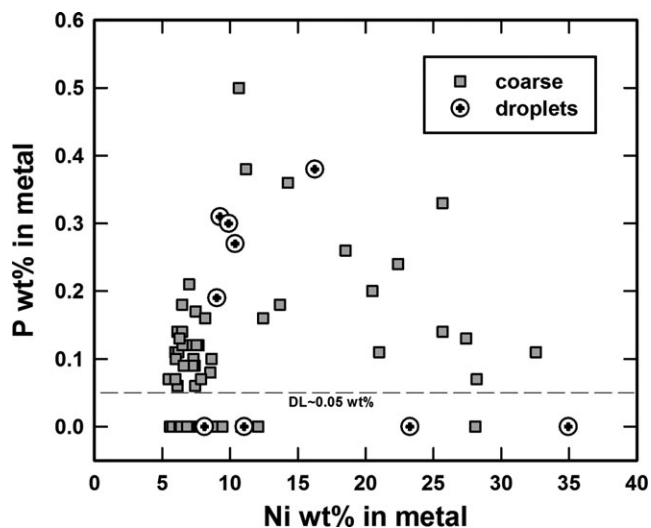


Fig. 14. Relationship of Ni and P contents in metal alloy from MIL 07273, based on SEM mapping data. Analyses have an apparent P detection limit (DL) of ~0.05 wt%. Although some analyses fall below this DL, many others are above it. Coarse grains and smaller droplets (globules and rounded grains) have a similar range of compositions (though droplets are more often P-enriched).

clinoenstatite on orthopyroxene clasts are relatively magnesian, with Fs values significantly lower than the H4–6 range (Fig. 11b). Matrix pyroxenes are enriched in Na and Al (Table 5), with up to 3 wt% Na<sub>2</sub>O and 8 wt% Al<sub>2</sub>O<sub>3</sub> (Figs. 13a and 13b). These soda and alumina contents roughly correlate with CaO or Wo contents in the pyroxenes (i.e., all are enriched in pigeonite), although lower-Ca pyroxenes that are probably clinoenstatite are also enriched in Na and Al compared with low-Ca pyroxene in clasts (Fig. 13). The Na-Al-rich matrix pigeonites approach ~30% of a jadeite (NaAlSi<sub>2</sub>O<sub>6</sub>) component and qualify as omphacite. High Na and Al contents of matrix pyroxene are evidently real and not an artifact of beam overlap with a Na-Al-rich phase, as there are often no other phases in the matrix surrounding the pyroxene grains that could be contributing the corresponding X-ray counts, and as mineral stoichiometry is consistent with pyroxene. Variations in Ca, Al, Na, and Cr contents in matrix pyroxene do not reflect any obvious grain zoning. Instead, judging from X-ray maps, grains have locally different compositions in different areas.

Matrix olivine is notably ferroan (Fa<sub>18–29</sub>) compared to that in chondrule clasts in MIL and compared to equilibrated H chondrites (Fig. 11a). BSE images indicate that olivine overgrowths on olivine mineral clasts have similar ferroan compositions (Fig. 5h). Analyses indicate apparently elevated Al, Ca, and Na contents for this olivine (Table 5), but in this

case, these values are almost certainly an artifact of contaminating X-ray generation in surrounding phases (i.e., pyroxene).

Although metal in MIL has an average composition similar to H chondrites, the compositions of the metal grains themselves are highly variable. Both coarse and matrix (rounded, apparent droplet) metal range widely in Ni content, from ~6 wt% (kamacite or martensite) to ~35 wt% (taenite), and are often significantly enriched in P, up to ~0.5 wt% (Fig. 14). For those analyses with P contents above the apparent detection limit of ~0.05 wt%, phosphorus concentrations tend to be higher in metal with intermediate Ni values (Fig. 14).

A striking chemical feature of metal is the presence of Ni-rich halos in martensite that surrounds taenite grains. These halos give the interiors of metal grains a diffuse appearance in Fe or Ni X-ray maps (Figs. 5l and 10b). Diffuse, slightly Ni-rich areas also occur in martensite where no central taenite is apparent.

Figure 9 shows Ni linescan data for a coarse metal particle that contains martensite, a few kamacite grains, and three taenite grains. The traverse data for this and other coarse metal particles reveal that (1) taenite (mainly ~21–29 wt% Ni) is chemically variable but does not have consistent grain core-rim zoning (Figs. 9d and 9e); (2) kamacite (mainly ~6 wt% Ni) does not have consistent core-rim zoning but can increase slightly in Ni content toward martensite (Fig. 9d); (3) martensite grains show systematic grain core-rim zoning, with Ni-poor cores (~6–8 wt% Ni typical) and narrow (~1–5  $\mu\text{m}$  wide) Ni-rich rims (~14 wt% Ni typical) (Figs. 9d and 9e); (4) Ni content in martensite surrounding taenite in a Ni-rich halo increases toward taenite, forming a band ~10–20  $\mu\text{m}$  wide (Figs. 9d and 9e); and (5) martensite has different compositions in different metal particles. One of the most Ni-rich coarse metal particles (Fig. 5l) contains martensite that has elevated Ni content throughout (grain core with ~10 wt% Ni, grain rim at edge of particle with ~26 wt% Ni, which here could be taenite), as well as an irregularly shaped taenite (~26 wt% Ni) surrounded by a broad and somewhat irregularly shaped Ni-rich halo, and no apparent (low-Ni) kamacite grains. Other coarse metal particles lack Ni-rich taenite/halo regions and are composed of martensite and/or kamacite alone.

### Geothermometry

Pyroxene geothermometry results are given in Table 6, assuming low-pressure (1 atm) equilibria. At higher pressure, corresponding temperatures are higher (Lindsley and Anderson 1983), so the values in Table 6 are lower limits. For instance, at pressures of 2 GPa, pigeonite

Table 6. Pyroxene geothermometry results for MIL 07273.<sup>a</sup>

Phase	Temperature (°C)
Orthopyroxene <sup>b</sup>	836 $\pm$ 47 ( <i>n</i> = 37)
Diopside <sup>c</sup>	976 $\pm$ 43 ( <i>n</i> = 15)
Diopside, subcalcic <sup>d</sup>	1213 $\pm$ 67 ( <i>n</i> = 3)
Pigeonite <sup>e</sup>	1253 $\pm$ 77 ( <i>n</i> = 14)

<sup>a</sup>Mean and  $\pm 1$  standard deviation of multiple SEM analyses (*n* = number of analyses) based on the 1 atm graphical pyroxene geothermometer of Lindsley (1983) and Lindsley and Anderson (1983).

<sup>b</sup>Low-Ca pyroxene (orthopyroxene) in clasts, excluding magnesian overgrowths (clinostatite), a discordant analysis (#132, apparent T ~1105 °C), and two analyses with Ca content below detection.

<sup>c</sup>Diopside in larger and smaller clasts, which yield apparent temperature ~895–1040 °C.

<sup>d</sup>Subcalcic diopside (augite) yielding apparent high temperature (1170–1290 °C) including two small clasts and one larger, temperatures approximate.

<sup>e</sup>Matrix pigeonite, temperatures approximate.

of a given composition could correspond to temperatures ~200 °C higher than at ~1 atm (Lindsley 1983).

Different pyroxene temperatures are obtained depending on the phase and petrographic context. Clearly the variety of geothermometer temperatures found in MIL (Table 6) requires disequilibrium overall, but as results correlate with petrographic setting, it is plausible that these variations reflect local equilibrium. Pyroxene minerals in clasts yield lower temperatures, mainly 810–880 °C (average ~840 °C) for orthopyroxene and 895–1040 °C (average ~980 °C) for most diopside (Table 6). Matrix pigeonite and a few subcalcic diopside (augite) analyses in clasts yield higher temperatures, ~1120–1360 °C (average ~1250 °C) for pigeonite and ~1170–1290 °C (average ~1210 °C) for subcalcic diopside (Table 6). Two of the subcalcic diopsides are of small clasts with blurred boundaries, which appear to be dissolving in matrix.

## DISCUSSION

### Chondritic Protolith and Relationship to Low-FeO Chondrites

One of the initial motivations for studying MIL 07273 was the possibility that it was a low-FeO chondrite (Weisberg et al. 2010). Although the exact definition of what constitutes a low-FeO chondrite is not firm, such chondrites appear to have lower FeO contents in mafic minerals than one would expect for an ordinary chondrite (Wasson et al. 1993; McCoy et al. 1994; Russell et al. 1998; Troiano et al. 2011), yet more-or-less resemble ordinary chondrites in other respects



(Wasson et al. 1993; Troiano et al. 2011). Our data show, however, that Fa and Fs contents in olivine and orthopyroxene from chondrule clasts in MIL overlap the range expected for H chondrites. This indicates that MIL 07273 is not a low-FeO chondrite.

Furthermore, there is good evidence that MIL was derived from the H chondrite parent body. Mineral compositions, bulk chemical composition, metal content, and bulk density are all most similar to H chondrites (see Results). Chondrule sizes too are most similar to H chondrites.

### Anomalous Melt Breccia Character of MIL 07273

MIL has some anomalous features. Among these is the oxygen isotopic composition, which falls outside of the usual ordinary chondrite groups (Fig. 1). Further, the porosity of the rock is remarkably low for an ordinary chondrite (Fig. 4). The shapes of coarser metal grains are unusual (Figs. 3 and 5a) and do not have a strong alignment in terms of their long axes, indicating they lack the foliation typical for shocked chondrites. MIL is obviously distinct in having a fine-grained but largely crystalline matrix and in having a troilite vein network that is responsible for blackening.

As discussed in more detail later, we interpret most of these anomalous features as reflecting a distinctive shock history, which included melting and crystallization of the matrix. Specifically, MIL 07273 is almost certainly impact melt breccia that contains clasts and a melt matrix. In this regard, it has the same classification as Shaw L6 (Taylor et al. 1979), Chico L6 (Bogard et al. 1995), Smyer (Rubin 2002), Rose City H5 (Rubin 1995), and Cat Mountain L5 (Kring et al. 1996). However, it differs from each of these. A lack of abundant feldspathic glass or mesostasis in the matrix of MIL 07273 distinguishes it from Chico (Bogard et al. 1995), Cat Mountain (Kring et al. 1996), Rose City (Rubin 1995), and Smyer (Rubin 2002). Two of three lithologies in Shaw also contain abundant feldspathic material, whereas the third is described as consisting of orthopyroxene poikilitically enclosing anhedral olivine grains (Taylor et al. 1979) and does not resemble what is found in MIL 07273.

Some meteorites with chemical affinity to ordinary chondrites are better described as clast-poor melt rocks and also differ from MIL 07273 both in overall texture and mineralogy. These include Yamato-790964 and Yamato-790143 (Okano et al. 1990; Yamaguchi et al. 1998), Ramsdorf (Yamaguchi et al. 1999), PAT 91501 (Mittlefehldt and Lindstrom 2001), Dar al Gani 896 (Folco et al. 2004), and MIL 05029 (Weirich et al. 2010). None of these are feldspar-poor melts similar to the matrix of MIL 07273.

### Melting and Crystallization of Matrix

The matrix of MIL 07273 differs from typical ordinary chondrite matrix, both the fine-grained porous assemblage of low-type (weakly metamorphosed) chondrites and the coarser granoblastic assemblage of high-type (strongly metamorphosed) chondrites. Evidence indicates that the matrix in MIL crystallized from a shock-produced melt. This includes (1) the compact texture of interlocking grains, which is consistent with a melt origin; (2) the presence of pigeonite, which is an igneous mineral; (3) the ubiquitous rounded metal and metal-troilite grains among matrix silicates, which were clearly produced as immiscible melt droplets; (4) geothermometry temperatures for matrix phases consistent with igneous temperatures (Table 6); and (5) low GOS values for minerals in matrix, unlike those in clasts, which can be explained by crystallization from shock melt entraining deformed clasts. The other chief matrix phase, clinoenstatite, could have formed by inversion of largely unquenchable pyroxene polymorphs that can crystallize at high temperature, including protopyroxene at low pressures (Deer et al. 1966; Huebner 1980) and high-P clinoenstatite at high pressures (Gasparik 1992; Presnall 1995; Ulmer and Stalder 2001).

We infer that matrix was melted because temperatures during shock were maximized there. This is consistent with numerical simulations which show that heating effects during impacts will be concentrated in porous matrix areas of chondrites (Bland et al. 2014). For example, projectiles moving at  $\geq 2.5 \text{ km s}^{-1}$  impacting ordinary chondrite-like targets with 30% porous matrix and a bulk porosity of 23% should result in total melting of matrix while leaving chondrules much less affected (Bland et al. 2014). Type 5 H, L, and LL ordinary chondrites with relatively high porosity (~10–20%) are known (Sasso et al. 2009), and we infer that an H5 chondrite at the upper end of this porosity range could have been a suitable precursor for MIL. Shock compaction with associated matrix melting was undoubtedly responsible for producing the anomalously low porosity measured for MIL as well as the high coherence of the rock.

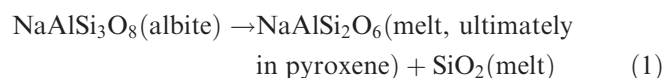
Textural evidence suggests matrix olivine largely crystallized after matrix pyroxene, resulting in olivine interstitial to coarser pyroxene. If fractional crystallization occurred in the melt matrix, it could explain why this olivine is more ferrous than olivine in chondrule clasts (Fig. 11a), as pyroxene would preferentially incorporate Mg over Fe during crystallization to leave a Fe-rich residual melt.

Conversely, the most magnesian phase in matrix is magnesian pyroxene (clinoenstatite) overgrowths on clasts (Figs. 11 and 12), which could have crystallized first at the highest temperature. This possible occurrence of fractional crystallization in matrix melt is supported by an interpretation for shock melt veins in the Peace River chondrite (Miyahara et al. 2008).

Both clinoenstatite and especially pigeonite in the matrix are enriched in a jadeite component (Fig. 13). Although fractional crystallization would tend to enrich later crystallizing matrix pigeonite in Na and Al, the very high contents of these elements are far outside the range encountered for normal terrestrial orthopyroxene, pigeonite, and Ca pyroxene (Robinson 1980) and require another explanation.

Jadeite of various textures has been found associated with either Si-rich glass or high-pressure silica polytypes (stishovite) in the shock melt veins of various chondrites (Kimura et al. 2000; Miyahara et al. 2013; Ozawa et al. 2014; Barzhan et al. 2017). It is interpreted to be the product of shock-induced albite breakdown at elevated pressures and temperatures either in the solid state (Miyahara et al. 2013) or following melting (Ozawa et al. 2014; Barzhan et al. 2017). However, the jadeite found in the shock melt veins of these chondrites is unlike the omphacitic pigeonite found in the matrix of MIL 07273, which is not jadeite *sensu stricto* and which is not associated with abundant feldspathic glass or a discrete silica phase.

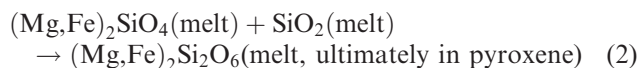
We suggest that matrix pyroxene incorporated a jadeite component from breakdown of albitic feldspar during melting, according to the following reaction:



Reaction 1 is supported by mass balance calculations, which suggest that Na and Al contents similar to that in matrix pigeonite can be produced by essentially complete removal of these elements from a chondrite-like proportion of albite. This in turn is consistent with the strong depletion of feldspathic phases in matrix (Table 4), which indicates removal of these phases during melting. Feldspar melts readily during disequilibrium melting of an ordinary chondrite (Feldstein et al. 2001), but the bulk Na and Al contents of MIL are close to average H chondrite, implying that a melted feldspar component was not lost but rather partly converted to something else.

Reaction 1 implies production of excess  $\text{SiO}_2$ . However, no silica phase was found in MIL, and feldspathic glasses in MIL do not contain sig-

nificant excess silica compared to feldspar. Instead, silica could have reacted with olivine melt to form the pyroxene-normative melt from which the matrix crystallized:



Reactions 1 and 2, operating together, can explain the high abundance of pyroxene and low proportions of feldspar and olivine in the matrix of MIL. Reaction 2 also could explain why no magnesian olivine overgrowths are found on olivine clasts, as any olivine that was melted would react to form pyroxene and would not crystallize immediately as olivine. However, olivine did crystallize in matrix at a later stage and clasts were overgrown by ferroan olivine similar in composition to that in the matrix. Thus, it is inferred that Reactions 1 and 2 stopped when feldspar was largely consumed, prior to the crystallization of matrix olivine.

### Incomplete Melting and Crystallization of Coarse Metal

Data for coarse metal in MIL are interpreted as indicating that such metal was largely, but incompletely, melted. The scalloped edges of metal and inclusion of other phases within it imply that metal readily filled spaces between silicates and other grains (chromite, phosphate), as could occur if the metal were liquid (Fig. 5k). Most of this metal is polycrystalline martensite and shows grain core-rim zoning of Ni, with narrow Ni-rich rims. The core-rim zoning is interpreted as having been created by fractional crystallization of metallic melt, as Ni is slightly incompatible and would be enriched in late-solidifying melt (Kubaschewski 2013). A similar observation and explanation for core-rim zoning in martensite was suggested for shock-reheated chondrites (Smith and Goldstein 1977) and for metal-troilite nodules in shock melted portions of the Yangzhuang (H6) chondrite (Ming et al. 1995).

A high-temperature origin for coarse metal is suggested by an overall similarity in Ni and P contents between metal in coarse phases and in metal-troilite globules, and specifically by the elevated P contents of this metal (Fig. 14). The globules occur among what is interpreted to have been melted silicate and are clearly immiscible melt droplets; their high-P contents can be explained by redistribution of P into metal from phosphate at high temperatures (e.g., Smith and Goldstein 1977; Ruzicka et al. 2005).

Some coarse metal particles contain ragged coarse crystals of taenite and kamacite (Figs. 5l and 10c), and

these show no evidence of having crystallized from the same metallic melts that led to martensite. These kamacite and taenite grains are interpreted as unmelted relicts. The irregular shapes of these grains are consistent with partial dissolution during melting. Further, crystal orientations for taenite are not obviously related to the enclosing martensite, as might otherwise be expected if martensite inverted from the taenite during subsolidus cooling (e.g., Yang et al. 2014). Taenite lacks consistent core-rim zoning but is surrounded by distinctive Ni-rich halos. These halos could have formed by Ni redistribution between metallic melt and entrained Ni-rich taenites, with the metallic melts solidifying as a second generation of metal (initially taenite, which inverted to martensite).

Overall Ni-P contents in metal (Fig. 14) are consistent with incomplete melting of metal in the reheating event that created the MIL melt breccia. Scatter of Ni-P contents implies disequilibrium, as could arise in part by a mixture of grains that crystallized from metallic melt during rapid cooling, and from solid grains that survived melting and formed under more slowly cooling conditions initially. We infer that martensite with intermediate Ni and high-P contents reflects a closer approach to high-temperature equilibrium, whereas kamacites and taenites of lower P content reflect a closer approach to low-temperature equilibrium. Elevated GOS values for martensite compared to kamacite and taenite are attributed to some combination of (1) removal of defects in kamacite and taenite by high-temperature annealing during immersion in metallic melt, and (2) deformation in martensite created by inversion from parent taenite crystals (Bogers and Burgers 1964; Krauss and Marder 1971).

### Concurrent Brecciation, Deformation, Melting, and Crystallization

Evidence suggests that MIL 07273 underwent plastic deformation, brecciation, melting, and crystallization that partly overlapped in time. MIL is predominantly clastic, with clasts set in a crystallized melt matrix. Melting was complete in matrix and extensive in coarse metal particles. We infer that troilite was completely melted, with most troilite solidifying in rims that partly surround metal, or in troilite-rich veins. The extensive vein network, and the low porosity and space-filling nature of minerals in the veins, can be explained by the solidification of melts that pervaded the rock. Additional evidence that vein troilite was molten is the physical connection of veins to coarse metal grains that were likely molten. Weak plastic deformation observed for troilite suggests it formed

after deformation had largely ceased, by crystallization from a late-stage melt as the rock cooled.

The tendency for different silicates to have different densities of troilite veins correlated with different degrees of plastic deformation suggests that chondrule clasts were partly melted. In the clasts, veins are most common in olivine, low-Ca pyroxene, and chromite and less common in diopside, feldspathic phases, and merrillite. Moreover, GOS values that measure plastic deformation are higher in coarse olivine and orthopyroxene and lower in minerals such as coarse diopside and feldspar. This suggests that olivine and orthopyroxene in chondrules were less melted, and diopside and feldspathic areas were more melted, during the deformation that created the MIL breccia. Moderate GOS values for feldspar, diopside, clinoenstatite, and pigeonite in chondrule clasts could indicate that they crystallized prior to complete cessation of deformation. Troilite vein liquids were concentrated in the less-melted minerals because injection of these liquids into pre-existing solids occurred prior to solidification of the melted silicates. Some olivine and merrillite recrystallized during deformation, and some orthopyroxene was transformed to clinoenstatite during deformation, with these transformations occurring after most veining. In general, the observations suggest that up to ~50% of MIL was melted during breccia formation.

Although it appears that most or all of the diopside and feldspar in chondrule clasts melted, evidently these phases re-solidified as new crystals with roughly the same compositions they had before melting. Feldspar is only slightly more calcic than typical for ordinary chondrites, and most diopside chemically resembles what is found in ordinary chondrites.

Geothermometry results for MIL orthopyroxene and diopside also suggest that these phases largely preserved their preshock compositions. For orthopyroxene and diopside in clasts, temperatures imply equilibration under subsolidus conditions, similar to what is found in metamorphosed type 6 ordinary chondrites (Slater-Reynolds and McSween 2005). This is despite a clearly atypical thermal history of MIL, which involved high peak temperatures for at least a brief period of time (discussed in the following section). Significant re-equilibration evidently did not occur owing to the brevity of the temperature spike and the sluggishness of diffusion relative to the cooling time scale. Similarly, there is no evidence that the composition of coarse olivine in chondrule clasts changed during shock reheating.

MIL shows evidence for a stress field that is reflected in the shapes of coarse metal grains and the bars of barred olivine chondrule clasts. Cone-shaped



coarse metal grains (Fig. 3, 5a) are interpreted as reflecting the flow of liquefied metal away from their convex sides toward their more irregular concave sides during passage of a shock wave. The same stress field could have been responsible for bending olivine bars in partly molten chondrules. In one well-studied example (Figs. 5f and 10), the curvature of the bars is in the same sense as the cone-shaped metal, and the microfaulting of the bars is consistent with a principal stress direction oriented roughly parallel to aligned cone-shaped metal grains (Figs. 5a and 5f). In a different relict chondrule, the olivine bars curve in the opposite sense, in this case curving around an adjacent relict chondrule that appears to have pushed into the bars.

### Presence of Gas

Although MIL has low porosity, the presence of apparent vesicles in feldspathic glass and the existence of larger intergranular voids suggest that gas was generated by shock heating.

That circular or oval holes with smooth outlines (Fig. 5i) are vesicles is consistent with their prevalence in glass, which could have formed by the solidification of a pressurized melt that later released gas. One vesicle was found at the edge of a crystalline feldspar area in a clast, which suggests gas release in melt prior to the crystallization of feldspar. However, crystalline feldspar grains in clasts that are broken and surrounded by melt matrix (Figs. 5j and 7) evidently crystallized before the cessation of brecciation. Thus, gas release could have occurred rather late but possibly before crystallization of feldspar and brecciation was complete.

Occasional large intergranular voids with irregular to circular outlines up to hundreds of microns across are found in tomogram image slices (Fig. 3a). These voids occur within the interior of the rock and cannot be explained as sample preparation artifacts. There are three possible explanations for these large cavities. They could represent either (1) areas where meteorite was dissolved and removed through cracks during terrestrial weathering; (2) original intergranular porosity that was not removed by shock compaction; or (3) vugs produced during outgassing, analogous to the small vesicles.

We argue that weathering and original porosity are both unlikely. Weathering is inconsistent with the low weathering grade of MIL as observed in thin section. It is also unreasonable to suppose that shock compaction and melting were effective at removing virtually all porosity in MIL except in a few localized areas that remained open as empty space.

A vug origin for the larger cavities is favored. This hypothesis is consistent with the presence of some

cavities elsewhere that are almost certainly vesicles and with curved outlines for some of the cavities (Fig. 3a), which could be the surfaces of gas bubbles. The general size and shape of the larger cavities in MIL are similar to vugs in the Yamato-790964 melt rock (Okano et al. 1990), but the cavities in MIL are much less numerous and prominent than vesicles and vugs reported for various ordinary chondrite melt breccias and melt rocks (Taylor et al. 1979; Okano et al. 1990; Yamaguchi et al. 1998).

### Pressure-Temperature Conditions of Shock Event

We suggest that although MIL ultimately solidified under low-pressure (P) conditions, pressures at the start of crystallization were considerably higher. With this hypothesis, high-P polymorphs in melt matrix transformed to low-P polymorphs upon cooling. Such back-transformations seem capable of occurring under certain conditions without entailing a significant change in mineral texture or composition, as evidenced from the Yamato-75267 chondrite (Kimura et al. 2003).

The omphacitic composition of matrix pigeonites allows an estimate of minimum pressures and temperatures for the initial heat pulse to create melt matrix. To break down feldspar and create a jadeitic pyroxene and silica melt, phase diagrams for the  $\text{NaAlSi}_3\text{O}_8$  system (e.g., Presnall [1995] and references therein) suggest that Reaction 1 would have occurred at elevated pressure (>3 GPa) and temperature (>1350 °C). This agrees with the minimum temperature stability for pigeonite of the appropriate Fe/Mg for MIL, which is >1250 °C at 1 atm and >1450 °C at 2 GPa (see Geothermometry section).

Other evidence implies that peak pressures and temperatures went higher. Shock experiments indicate that shock stage S4, as inferred for clasts in MIL, corresponds to a peak pressure of 20–30 GPa (Schmitt and Stöffler 1995; Schmitt 2000). These experiments used a somewhat porous (9%) H6 chondrite (Kernouvé) precursor, and the postshock temperature for this shock stage was calculated as ~540–660 K (~270–390 °C) (Schmitt 2000), which is insufficient for melting. However, if heating effects were concentrated in matrix owing to higher initial porosity, the matrix could have melted and left chondrules deformed and partly unmelted. Numerical simulations indicate that although peak temperatures could have been much higher in matrix than in chondrule areas, peak pressures would have been only slightly higher in matrix (Bland et al. 2014). Thus, if the pressure calibration of dynamic experiments is applicable to MIL, a shock stage of S4 for the chondrule clasts implies that pressures could have reached 20–30 GPa in the melt matrix.

Textures in MIL matrix suggest that pyroxene was a liquidus phase and olivine a near-solidus phase, unlike what one would expect for a chondritic melt at low *P*. However, experiments on peridotite and chondrite compositions show that between ~14 and 24–25 GPa, high-*P* pyroxene polytypes (majorite garnet or majorite-pyroxene garnet) appear on the liquidus and high-*P* polymorphs of olivine (wadsleyite or ringwoodite) appear near the solidus (Ohtani 1987; Agee et al. 1995; Herzberg and Zhang 1996; Asahara et al. 2004). Magnesiowüstite ([Mg,Fe]O) appears as a second phase in the liquid + solid field between 19 and 25 GPa (Herzberg and Zhang 1996; Asahara et al. 2004) and is unlike any phase found in MIL. But between ~15–16 and ~19 GPa, only polytypes of pyroxene (garnet) and olivine (wadsleyite) are present from the liquidus to well below the solidus (Herzberg and Zhang 1996). If MIL reached melting conditions at such high pressures, temperatures in the melting range could have been up to ~2200 °C for a peridotite composition (Herzberg and Zhang 1996) or down to ~1800 °C for a possibly more relevant Allende chondrite composition (Agee et al. 1995; Gillet et al. 2007), or roughly  $\geq 2000$  °C.

Phase compositions of omphacitic pigeonite in MIL matrix also resemble those of high-*P* phases in experiments and shock veins. This includes elevated Ca and Al contents for garnets in 15.5 GPa experiments (Herzberg and Zhang 1996), and elevated Na and Al contents for high-*P* pyroxene polytypes in the shock veins of L and H chondrites (Gillet et al. 2007) including majorite-pyroxene (Chen et al. 1996, 2004; Kimura et al. 2003; Ohtani et al. 2004) and akimotoite ([Mg,Fe]SiO<sub>3</sub> with ilmenite structure) (Sharp et al. 1997; Tomioko and Fujino 1999; Xie and Sharp 2004; Ferrier et al. 2008). Moreover, textures, grain sizes, and compositions of akimotoite and ringwoodite in shock veins from Umbarger (L6) (Xie and Sharp 2004) are all similar to MIL, except that olivine takes the place of ringwoodite, and pigeonite or clinoenstatite takes the place of akimotoite. Ringwoodite in Umbarger is somewhat more FeO-rich than olivine in the coexisting host (Xie and Sharp 2004), again paralleling the situation found in MIL.

Thus, the texture and phase chemistry of matrix minerals in MIL are consistent with back-transformation of high-*P* phases produced at high pressures (~15–19 GPa) and temperatures ( $\geq 2000$  °C) in matrix initially. For comparison, simulations of impacts with projectile speed of 3 km s<sup>-1</sup> into an ordinary chondrite target with a porous matrix fraction of 30% and initial bulk porosity of 23%, sufficient to cause complete melting of matrix, would involve a peak shock *P* of ~20–30 GPa and a bulk shock *P* of  $\leq 20$  GPa (Bland et al. 2014), which is similar to the ~20–30 GPa

estimated for shock stage S4 (Schmitt 2000). These estimates all converge and are consistent with the observations for MIL. For MIL, therefore, we speculate that (1) pigeonite, (2) clinoenstatite, and (3) olivine in the matrix formed by respective back-reaction of (1) majorite-pyroxene or akimotoite, (2) majorite, and (3) wadsleyite or ringwoodite. However, additional work is needed to confirm these transformations for MIL.

Regardless of the exact maximum pressure and temperature experienced by MIL, ultimately both decreased following the passage of the shock wave. If gas was generated in MIL as a result of heating, it likely would have been formed and released at a relatively late stage following depressurization, while melt was still present. Thus, MIL would have reached low pressure before solidification was complete.

### Thermal History

The low-pressure mineralogy in MIL and evidence for inversion of high-*P* polytypes during cooling suggests that MIL could have followed a cooling path that allowed high temperatures to persist for a longer period of time, compared to a pressure path that involved a quick drop from peak pressure conditions.

Constraints on the cooling history for MIL can be obtained from compositional variations in the coarse metal phases. This includes Ni-rich halos around taenite, which were likely produced by exchange between taenite and liquid metal; and zoned martensite grains, which were likely produced by fractional crystallization of metal from metallic melt. Although the Ni-rich halos were probably produced by a combination of dissolution and diffusion in metallic melt, an upper limit to cooling time under melt conditions can be obtained by assuming that their widths reflect only diffusion in liquid metal. Similarly, although Ni zonation in taenite was likely the result of fractional crystallization, a lower limit to cooling rate can be obtained assuming that diffusion in metal would broaden Ni-rich rims.

Order-of-magnitude time scales were calculated from the formula  $t \sim x^2/D$  (where  $t$  = time,  $x$  = diffusion length, and  $D$  = diffusion coefficient), and cooling times and cooling rates were estimated by combining results at different temperatures. Melting temperatures corresponding to low pressures were assumed (i.e., a metal liquidus of ~1500 °C; Kubaschewski 2013), which could be justified if pressure release occurred rapidly. Two different sets of diffusion coefficients in metal were used (Heyward and Goldstein 1973; Million et al. 1981), but these did not give significantly different results for the temperatures of interest.

Results are summarized in Table S4 in supporting information. To create a 10- to 20- $\mu$ m-wide Ni halo in

metallic melt, ~25–100 ms is needed just above the liquidus at 1500 °C, with a best estimate of ~56 ms (a 15- $\mu$ m-wide halo). These durations are upper limits, as halos were probably partly produced by dissolution. This indicates a duration of <100 ms and probably <56 ms at ~1500 °C to create the halos, which implies very rapid heating and cooling at that temperature. Even shorter time scales and faster cooling rates are implied for higher temperatures, as diffusion rates would have been higher. Considering that Ni-rich grain rims on martensite are ~3  $\mu$ m wide on average, cooling from 1500 to 1400 °C would have had to occur in <1 minute, and cooling to 1000 °C would have had to occur in <4–5 hours, so as to prevent diffusion over a larger length scale. These time scales correspond roughly to cooling rates of 1–2 °C s<sup>-1</sup> at >1300 °C and to ~40–90 °C h<sup>-1</sup> at 1000 °C. With such cooling rates, Ni halos are not significantly “smeared” by diffusion in solid metal, i.e., the cooling rates would have to be much slower to create the observed chemical variation. Thus, one can infer that if Ni halos were created in metallic melt, diffusion in subsequently crystallized metal would not significantly alter their chemical profiles.

However, these results allow the possibility of much slower cooling rates as temperatures approached ~1000 °C. The latter temperatures are just above the metal-troilite solidus ( $\leq$ 990 °C; Usselman 1975; Kubaschewski 2013) and somewhat below the silicate solidus of  $\leq$ 1150 °C (Jurewicz et al. 1993, 1995). This suggests that metallic melt in MIL could have been present for hours, well after the silicates in matrix and elsewhere had solidified. Given that low-temperature metallic melts should be S-rich (Kubaschewski 2013), veins of troilite conceivably could have formed late, if gas pressure or some other mechanism promoted melt transport. This might explain the existence of troilite veins that cross both clasts and matrix areas (Figs. 5i and 8).

### The Puzzling Oxygen Isotope Composition of MIL 07273

The oxygen isotopic composition of MIL is a puzzle. Despite evidence that the protolith was an H chondrite, MIL has  $\Delta^{17}\text{O}$  values too high for H and more consistent with an L-group chondrite, although  $\delta^{18}\text{O}$  values are low for an L chondrite and more like an H chondrite (Fig. 1). Here, we discuss different explanations for the O-isotopic composition of MIL. This composition in principle could (1) be in error; (2) have been shifted from an H chondrite composition by terrestrial weathering; (3) reflect impact mixing between an H target and a projectile with different composition;

(4) indicate derivation of MIL from an L chondrite protolith, with other properties of MIL transformed from L to appear more H like; or (5) reflect impact vaporization.

We discount that the composition is in error, because of consistency in  $\Delta^{17}\text{O}$  values between five different aliquots analyzed in two different laboratories. The standard deviation in  $\Delta^{17}\text{O}$  values for the five analyses is only 0.02‰ (Table 1). A larger variation in  $\delta^{18}\text{O}$  and  $\delta^{17}\text{O}$  (Table 1, Fig. 1) can be explained by mass-dependent fractionation, such as might occur by analyzing aliquots with different mineral proportions. Thus, the oxygen isotope results likely reflect the true composition of MIL.

Terrestrial weathering of an H chondrite is also discounted as a viable explanation. This process would be expected to shift  $\Delta^{17}\text{O}$  values lower, toward the terrestrial mass fractionation (TF) line (e.g., Bland et al. 2000), but the  $\Delta^{17}\text{O}$  values for MIL are instead shifted *away* from the TF line. Moreover, the weathering grade for MIL is low, at the low end of grade W1. For terrestrial weathering, oxygen isotope compositions are significantly changed only for high degrees of weathering (Bland et al. 2000). Furthermore, there is no evidence from the bulk chemical composition of MIL for strong weathering effects. Finally, both analysis protocols used to determine oxygen isotope compositions involved cleaning steps to remove whatever terrestrial weathering products might be present.

Impact mixing also seems unlikely to account for the observed shift from H. The only known impactors that could be mixed with an H chondrite target to give the oxygen isotopic composition measured for MIL are L, LL, or R chondrites, assuming that they in addition were also mass-fractionated to lower  $\delta^{18}\text{O}$  (e.g., Weisberg et al. 2006). All of these impactor types are more oxidized (higher FeO and lower metal contents) than H (e.g., Weisberg et al. 2006), and would be expected to perturb Fa, Fs, and metal contents from H in a resulting mixture, so as to lie on mixing lines. But for MIL, there is no evidence that these values are significantly different from H chondrite.

Could MIL have been derived from an L protolith and chemically changed to look more like an H chondrite? In favor of this is that the  $\Delta^{17}\text{O}$  values for MIL are similar to typical L chondrite values and could lie on a mass fractionation trend for L chondrite, shifted to isotopically lighter values (Fig. 1). To chemically transform L chondrite into MIL, FeO and metal contents would have to decrease and increase, respectively. This could be done by a redox process such as:





However, Reaction 3 cannot explain H-like bulk abundances of multiple siderophile elements (Fig. 2b). Further, there is no evidence that silicates in MIL experienced FeO reduction. Olivine clasts lack FeO-poor rims, and matrix olivine that crystallized from melt is more, not less, ferroan (Fig. 11a). Thus, we discount the possibility that MIL is a transformed L chondrite.

Finally, the O-isotopic composition of MIL could have been shifted from H chondrite by the impact process that created the melt breccia. Vapor appears to have been lost from vesicles and vugs, and in principle, this could result in a change of the O-isotope composition of the analyzed residue. Indeed, intense heating of chondrites should lead to vaporization (Gooding and Muenow 1977; Muenow et al. 1995), and mass-dependent fractionations involving loss of isotopically light oxygen-bearing gas by impact vaporization are expected on theoretical grounds (Housley 1979) and observed for lunar materials (Clayton et al. 1974). However, to explain the data for MIL requires a *mass-independent* fractionation in oxygen. So far as we are aware, no mass-independent fractionation for oxygen of the sort required for MIL has been suggested for an impact process.

Thus, we do not have a good explanation for the measured oxygen isotopic composition of MIL. However, we can conclude that it likely represents the true composition of MIL; that it does not reflect terrestrial weathering, impact mixing, or derivation from an L-group precursor; and that it does not fit the expectation for mass-dependent fractionation by impact vaporization.

## CONCLUSIONS

1. Miller Range 07273 is a melt breccia with clasts of chondrules set in a largely crystalline, igneous-textured matrix. It represents a relatively uncommon but potentially important rock type that has been poorly studied.
2. Contrary to preliminary indications, MIL 07273 does not belong to a low-FeO group of ordinary chondrite.
3. MIL was likely produced by an impact on the H group parent body, which resulted in deformation, melting, brecciation, and crystallization. The relative importance of these processes varied by location and mineral. Some vaporization also may have occurred.
4. The matrix was completely melted, and chondrule clasts were themselves partly melted. Molten troilite was extensively mobilized into a vein network, with veins concentrated in olivine, orthopyroxene, and chromite because these phases were less melted; ~50% of the MIL progenitor could have been melted.
5. Different silicates show variable amounts of plastic deformation as quantified by grain orientation spread (GOS). GOS values are highest in coarse olivine, with ~4–5° of average misorientation, corresponding to an optically determined weighted shock stage of S4.0. In contrast, GOS values are very low (<1° and often ~0.3°, which is close to the detection limit) in troilite and matrix minerals (clinoenstatite, pigeonite, olivine), consistent with the crystallization of these minerals following deformation.
6. Metallic melt formed coarser liquefied patches that flowed in response to a stress field, producing cone shapes, as well as smaller immiscible droplets (metal-troilite globules and smaller blebs) in melted silicate areas. Metal crystallized to ultimately form martensite, although taenite and kamacite in coarser metal particles are best explained as unmelted relicts.
7. Melting and shock compression resulted in a very low porosity for MIL. Heating was likely concentrated in matrix as a result of high porosity in the chondritic (possibly H5) protolith.
8. Matrix pigeonites approach ~30% of a jadeite component and qualify as omphacite. These compositions are explained by the breakdown of albitic feldspar during melting to form a jadeite component, which could have involved elevated pressures (>3 GPa) and temperatures (>1350 °C).
9. Various characteristics of matrix suggest that shock pressures and temperatures could have been very high in MIL. Pressures may have reached ~15–19 GPa and temperatures ≥2000 °C, with matrix pyroxene and olivine possibly forming by back-transformation of high-P polytypes (e.g., majorite-pyroxene, akimotoite, majorite, wadsleyite) that crystallized at high pressure.
10. MIL likely experienced a brief spike in pressure and temperature, followed by a sharp drop in pressure and a more gradual decrease in temperature. Compositional variations in coarse metal suggest <100 ms at 1500 °C, with a cooling rate on the order of 1–2 °C s<sup>-1</sup> at >1300 °C, and possibly as slow as ~40–90 °C h<sup>-1</sup> at 1000 °C.
11. Despite extensive heating and even melting, the composition of silicates outside of matrix areas was not changed significantly during the shock event that created the melt breccia. This implies that intense but brief heating events can leave mineral compositions relatively unaffected.

12. The oxygen isotopic composition of MIL is most similar to H and L chondrites but falls outside of the fields established for these chondrites. This composition is puzzling, but it probably is not in error.

*Acknowledgments*—The authors thank Akira Yamaguchi, an anonymous reviewer, and Dr. Alan Rubin for comments that improved the quality of the manuscript. We also thank ANSMET, Johnson Space Center curation, and the Meteorite Working Group for collecting, sectioning, and distributing samples of Miller Range 07273. AMR thanks NASA for recent grant support that helped make this research possible (grants NNX10AH33G and NNX12ZDA001N from the Origins, Planetary Major Equipment, and Cosmochemistry programs), as well as discussions with Dr. Richard Hugo. JMF thanks the Camille and Henry Dreyfus Special Grant Program in the Chemical Sciences for providing vital material support. DSE acknowledges grant support from NASA (NNX16AD37G, Emerging Worlds program). Portions of this work were performed at GeoSoilEnviroCARS (Sector 13), Advanced Photon Source (APS), Argonne National Laboratory. GeoSoilEnviroCARS is supported by the National Science Foundation—Earth Sciences (EAR-1128799) and Department of Energy-GeoSciences (DE-FG02-94ER14466). This research used resources of the Advanced Photon Source, a U.S. Department of Energy (DOE) Office of Science User Facility operated for the DOE Office of Science by Argonne National Laboratory under Contract No. DE-AC02-06CH11357.

*Editorial Handling*—Dr. Akira Yamaguchi

## REFERENCES

- Agee C. B., Li J., Shannon C., and Circone S. 1995. Pressure-temperature phase diagram for the Allende meteorite. *Journal of Geophysical Research* 100:17725–17740.
- Anders E. and Grevesse N. 1989. Abundances of the elements: Meteoritic and solar. *Geochimica et Cosmochimica Acta* 53:197–214.
- Asahara Y., Kubo T., and Kondo T. 2004. Phase relations of a carbonaceous chondrite at lower mantle conditions. *Physics of Earth and Planetary Interiors* 143–144:421–432.
- Barzhan I. S., Ozawa S., Miyahara M., Ohtani E., and Litasov K. D. 2017. “Spherulite-like” jadeite growth in shock-melt veins of the Novosibirsk H5/6 chondrite. *Russian Geology and Geophysics* 58:12–19.
- Bland P. A., Lee M. R., Sexton A. S., Franchi I. A., Fallick A. E. T., Miller M. F., Cadogan J. M., Berry F. J., and Pillinger C. T. 2000. Aqueous alteration without a pronounced oxygen-isotopic shift: Implications for the asteroidal processing of chondritic materials. *Meteoritics & Planetary Science* 35:1387–1395.
- Bland P. A., Collins G. S., Davison T. M., Abreu N. M., Ciesla F. J., Muxworthy A. R., and Moore J. 2014. Pressure-temperature evolution of primordial solar system solids during impact-induced compaction. *Nature Communications* 5:541.
- Bogard D. D., Garrison D. H., Norman M., Scott E. R. D., and Keil K. 1995.  $^{39}\text{Ar}$ - $^{40}\text{Ar}$  age and petrology of Chico: Large-scale impact melting on the L chondrite parent body. *Geochimica et Cosmochimica Acta* 59:1383–1399.
- Bogers A. J. and Burgers W. G. 1964. Partial dislocations on the 110 planes in the BCC lattice and the transition of the FCC into the BCC lattice. *Acta Metallurgica* 12:255–261.
- Brearely A. J. and Jones R. H. 1998. Chondritic meteorites. In *Planetary materials*, edited by Papike J. J. Reviews in Mineralogy, vol. 36. Washington, D.C.: Mineralogical Society of America. pp. 3/1–3/398.
- Brewer L. N., Field D. P., and Merriman C. C. 2009. Mapping and assessing plastic deformation using EBSD. In *Electron backscatter diffraction in materials science*, edited by Schwartz A. J., Kumar M., Adams B. L., and Field D. P. New York: Springer. pp. 251–262.
- Chen M. and El Goresy A. 2000. The nature of maskelynite in shocked meteorites: Not diaplectic glass but a glass quenched from shock-induced dense melt at high pressures. *Earth and Planetary Science Letters* 179:489–502.
- Chen M., Sharp T. G., El Goresy A., Wopneka B., and Xie X. 1996. The majorite-pyrope + magnesiowustite assemblage: Constraints on the history of shock veins in chondrites. *Science* 271:1570–1573.
- Chen M., Xie X., and El Goresy A. 2004. A shock-produced (Mg, Fe)SiO<sub>3</sub> glass in the Suizhou meteorite. *Meteoritics & Planetary Science* 39:1797–1808.
- Clayton R. N., Mayeda T. K., and Hurd J. M. 1974. Loss of oxygen, silicon, sulfur, and potassium from the lunar regolith. Proceedings, 5th Lunar Science Conference. pp. 1801–1809.
- Clayton R. N., Mayeda T. K., Goswami J. N., and Olsen E. J. 1991. Oxygen isotope studies of ordinary chondrites. *Geochimica et Cosmochimica Acta* 55:2317–2337.
- Consolmagno G. J., Britt D. T., and Macke R. J. 2008. The significance of meteorite density and porosity. *Chemie der Erde* 68:1–29.
- Deer W. A., Howie R. A., and Zussman J. 1966. *An introduction to the rock forming minerals*. London: Longman Group. 528 p.
- Feldstein S. N., Jones R. H., and Papike J. J. 2001. Disequilibrium partial melting experiments on the Leedey L6 chondrite: Textural controls on melting processes. *Meteoritics & Planetary Science* 36:1421–1441.
- Ferrior T., Beck P., Van de Moortèle B., Bohn M., Reynard B., Simionvici A., El Goresy A., and Gillet P. 2008. Akimotoite in the Tenham meteorite: Crystal chemistry and high-pressure transformation mechanisms. *Earth and Planetary Science Letters* 275:26–31.
- Folco L., Bland P. A., D’Orazio M., Franchi I. A., Kelley S. P., and Rocchi S. 2004. Extensive impact melting on the H-chondrite parent asteroid during the cataclysmic bombardment of the early solar system: Evidence from the achondritic meteorite Dar al Gani 896. *Geochimica et Cosmochimica Acta* 68:2379–2397.
- Friedrich J. M. and Rivers M. L. 2013. Three-dimensional imaging of ordinary chondrite microporosity at 2.6 micrometer resolution. *Geochimica et Cosmochimica Acta* 116:63–70.

- Friedrich J. M., Wang M.-S., and Lipschutz M. E. 2002. Comparison of the trace element composition of Tagish Lake with other primitive carbonaceous chondrites. *Meteoritics & Planetary Science* 37:677–686.
- Friedrich J. M., Wignarajah D. P., Chaudhary S., Rivers M. L., Nehru C. E., and Ebel D. S. 2008. Three-dimensional petrography of metal phases in equilibrated L chondrites—Effects of shock loading and dynamic compaction. *Earth and Planetary Science Letters* 275:172–180.
- Friedrich J. M., Ruzicka A., Rivers M. L., Ebel D. S., Thostenson J. O., and Rudolph R. A. 2013. Metal veins in the Kernouvé (H6 S1) chondrite: Evidence for pre- or syn-metamorphic shear deformation. *Geochimica et Cosmochimica Acta* 116:71–83.
- Friedrich J. M., Weisberg M. K., and Rivers M. L. 2014. Multiple impact events recorded in the NWA 7298 H chondrite breccia and the dynamical evolution of an ordinary chondrite asteroid. *Earth and Planetary Science Letters* 394:13–19.
- Friedrich J. M., Weisberg M. K., Ebel D. S., Biltz A. E., Corbett B. M., Iotzov I. V., Khan W. S., and Wolman M. D. 2015. Chondrule size and related physical properties: A compilation and evaluation of current data across all meteorite groups. *Chemie der Erde—Geochemistry* 75:419–443.
- Friedrich J. M., Ruzicka A., Macke R. J., Thostenson J. O., Rudolph R. A., Rivers M. L., and Ebel D. S. 2017. Relationships among physical properties as indicators of high temperature deformation or post-shock thermal annealing in ordinary chondrites. *Geochimica et Cosmochimica Acta* 203:157–174.
- Gasparik T. 1992. Melting experiments on the enstatite-pyroxene join at 80–152 kbar. *Journal of Geophysical Research* 97:15181–15188.
- Gillet P., El Goresy A., Beck P., and Chen M. 2007. High-pressure mineral assemblages in shocked meteorites and shocked terrestrial rocks: Mechanisms of phase transformations and constraints to pressure and temperature histories. In *Advances in high-pressure mineralogy*, edited by Ohtani E. *Geological Society of America Special Paper* 421:57–82.
- Gooding J. L. and Muenow D. W. 1977. Experimental vaporization of the Holbrook chondrite. *Meteoritics* 12:401–408.
- Herzberg C. and Zhang J. 1996. Melting experiments on anhydrous peridotite KLB-1: Compositions of magma in the upper mantle and transition zone. *Journal of Geophysical Research* 101:8271–8295.
- Heyward T. R. and Goldstein J. I. 1973. Ternary diffusion in the  $\alpha$  and  $\gamma$  phases of the Fe-Ni-P system. *Metallurgical Transactions* 4:2335–2342.
- Housley R. M. 1979. A model for chemical and isotopic fractionation in the lunar regolith by impact vaporization. Proceedings, 10th Lunar and Planetary Science Conference. pp. 1673–1683.
- Huebner J. S. 1980. Pyroxene phase equilibria at low pressure. In *Pyroxenes*, edited by Prewitt C. T. Reviews in Mineralogy, vol. 7. Washington, D.C.: Mineralogical Society of America. pp. 213–288.
- Jamsja N. and Ruzicka A. 2010. Shock and thermal history of NWA 4859, an annealed impact-melt breccia of LL-chondrite parentage containing unusual igneous features and pentlandite. *Meteoritics & Planetary Science* 45:828–849.
- Jarosewich E. 1990. Chemical analyses of meteorites: A compilation of stony and iron meteorite analyses. *Meteoritics* 25:323–337.
- Jurewicz A. J. G., Mittlefehldt D. W., and Jones J. H. 1993. Experimental partial melting of the Allende (CV) and Murchison (CM) chondrites and the origin of asteroidal basalts. *Geochimica et Cosmochimica Acta* 57:2123–2139.
- Jurewicz A. J. G., Mittlefehldt D. W., and Jones J. H. 1995. Experimental partial melting of the St. Severin (LL) and Lost City (H) chondrites. *Geochimica et Cosmochimica Acta* 59:391–408.
- Kallemeyn G. W., Rubin A. E., Wang D., and Wasson J. T. 1989. Ordinary chondrites—Bulk compositions, classification, lithophile-element fractionations, and composition-petrographic type relationships. *Geochimica et Cosmochimica Acta* 53:2747–2767.
- Kimura M., Suzuki A., Kondo T., Ohtani E., and El Goresy A. 2000. Natural occurrence of high-pressure phases, jadeite, hollandite, wadsleyite and majorite-pyroxene garnet, in an H-chondrite, Y75100. *Meteoritics & Planetary Science* 35:A87–A88.
- Kimura M., Chen M., Yoshida Y., El Goresy A., and Ohtani E. 2003. Back-transformation of high-pressure phases in a shock melt vein of an H-chondrite during atmospheric passage: Implications for the survival of high-pressure phases after decompression. *Earth and Planetary Science Letters* 217:141–150.
- Krauss G. and Marder A. R. 1971. The morphology of martensite in iron alloys. *Metallurgical Transactions* 2:2343–2357.
- Kring D. A., Swindle T. D., Britt D. T., and Grier J. A. 1996. Cat Mountain: A meteoritic sample of an impact-melted asteroidal regolith. *Journal of Geophysical Research* 101:29,353–29,371.
- Kubaschewski O. 2013. *Iron—Binary phase diagrams*. Berlin/Heidelberg: Springer Science & Business Media.
- Lindsley D. H. 1983. Pyroxene thermometry. *American Mineralogist* 68:477–493.
- Lindsley D. H. and Anderson D. J. 1983. A two-pyroxene geothermometer. Proceedings, 13th Lunar and Planetary Science Conference. *Journal of Geophysical Research Supplement* 88:A887–A906.
- McCoy T. J., Keil K., Scott E. R. D., Benedix G. K., Ehlmann A. J., Mayeda T. K., and Clayton R. N. 1994. Low-FeO ordinary chondrites: A nebular origin and new chondrite parent body. 15th Lunar and Planetary Science Conference. p. 865.
- Meteoritical Bulletin Database*. 2016. <http://www.lpi.usra.edu/meteor/>. Accessed October 22, 2016.
- Million B., Růžicková J., Velišek J., and Vřešťál J. 1981. Diffusion processes in the Fe-Ni system. *Materials Science and Engineering* 50:43–52.
- Ming C., Xiande X., and El Goresy A. 1995. Nonequilibrium solidification and microstructures of metal phases in the shock-induced melt of the Yanzhuang (H6) chondrite. *Meteoritics* 30:28–32.
- Mittlefehldt D. W. and Lindstrom M. M. 2001. Petrology and geochemistry of Patuxent Range 91501, a clast-poor impact melt from the L-chondrite parent body and Lewis Cliff 88663, an L7 chondrite. *Meteoritics & Planetary Science* 36:439–457.
- Miyahara M., El Goresy A., Ohtani E., Nagse T., Nishijima M., Vashaei Z., Ferrier T., Gillet P., Dubrovinski L., and Simionovici A. 2008. Evidence for fractional crystallization



- of wadleyite and ringwoodite from olivine melts in chondrules entrained in shock melt veins. *Proceedings of the Natural Academy of Sciences* 105:8542–8547.
- Miyahara M., Ozawa S., Ohtani E., Kimura M., Kubo T., Sakai T., Nagase T., Nishijima M., and Hirao N. 2013. Jadeite formation in shocked ordinary chondrites. *Earth and Planetary Science Letters* 373:102–108.
- Muenow D. W., Keil K., and McCoy T. J. 1995. Volatiles in unequilibrated ordinary chondrites: Abundances, sources and implications for explosive volcanism on differentiated asteroids. *Meteoritics* 30:639–645.
- Ohtani E. 1987. Ultrahigh-pressure melting of a model chondritic mantle and pyrolite compositions. In *High-pressure research in mineral physics*, edited by Manghnami M. H. and Syono Y. Washington, D.C.: American Geophysical Union. pp. 87–93.
- Ohtani E., Kimura Y., Kimura M., Takata T., Kondo T., and Kubo T. 2004. Formation of high-pressure minerals in shocked L6 chondrite Yamato 791384: Constraints on shock conditions and parent body size. *Earth and Planetary Science Letters* 227:505–515.
- Okano O., Nakamura N., and Nagao K. 1990. Thermal history of the shock-melted Antarctic LL-chondrites from the Yamato-79 collection. *Geochimica et Cosmochimica Acta* 54:3509–3523.
- Ozawa S., Miyahara M., Ohtani E., Koroleva O. N., Ito Y., Litasov K. D., and Pokhilenko N. P. 2014. Jadeite in Chelyabinsk meteorite and the nature of an impact event on its parent body. *Scientific Reports* 4:1–5.
- Presnall D. C. 1995. Phase diagrams of Earth-forming minerals. In *Mineral physics and crystallography: A handbook of physical constants*, edited by Ahrens T. J. Washington, D.C.: American Geophysical Union. pp. 248–268.
- Robinson P. 1980. The composition space of terrestrial pyroxenes—internal and external limits. In *Pyroxenes*, edited by Prewitt C. T. Reviews in Mineralogy, vol. 7. Washington, D.C.: Mineralogical Society of America. pp. 419–494.
- Rubin A. E. 1995. Fractionation of refractory siderophile elements in metal from the Rose City meteorites. *Meteoritics* 30:412–417.
- Rubin A. E. 2002. Smyer H-chondrite impact-melt breccia and evidence for sulfur vaporization. *Geochimica et Cosmochimica Acta* 66:699–711.
- Russell S. S., McCoy T. J., Jarosewich E., and Ash R. D. 1998. The Burnwell, Kentucky, low iron oxide chondrite fall: Description, classification and origin. *Meteoritics & Planetary Science* 33:853–856.
- Ruzicka A., Killgore M., Mittlefehldt D. W., and Fries M. D. 2005. Portales Valley: Petrology of a metallic-melt meteorite breccia. *Meteoritics & Planetary Science* 40:261–295.
- Ruzicka A., Hugo R., and Hutson M. 2015. Deformation and thermal histories of ordinary chondrites: Evidence for post-deformation annealing and syn-metamorphic shock. *Geochimica et Cosmochimica Acta* 163:219–233.
- Sasso M. R., Macke R. J., Boesenberg J. S., Britt D. T., Rivers M. L., Ebel D. S., and Friedrich J. M. 2009. Incompletely compacted equilibrated ordinary chondrites. *Meteoritics & Planetary Science* 44:1743–1753.
- Schmitt R. T. 2000. Shock experiments with the H6 chondrite Kernouvé: Pressure calibration and microscopic shock effects. *Meteoritics & Planetary Science* 35:545–560.
- Schmitt R. T. and Stöffler D. 1995. Experimental data in support of the 1991 shock classification of chondrites. *Meteoritics & Planetary Science* 30:574–575.
- Sharp T. G., Lingemann C. M., Dupas C., and Stöffler D. 1997. Natural occurrence of MgSiO<sub>3</sub>-ilmenite and evidence for MgSiO<sub>3</sub>-pervoskite in a shocked L chondrite. *Science* 277:352–355.
- Slater-Reynolds V. and McSween H. Y. Jr. 2005. Peak metamorphic temperatures in type 6 ordinary chondrites: An evaluation of pyroxene and plagioclase geothermometry. *Meteoritics & Planetary Science* 40:745–754.
- Smith B. A. and Goldstein J. I. 1977. The metallic microstructures and thermal histories of severely reheated chondrites. *Geochimica et Cosmochimica Acta* 41:1061–1072.
- Stöffler D., Keil K., and Scott E. R. D. 1991. Shock metamorphism of ordinary chondrites. *Geochimica et Cosmochimica Acta* 55:3845–3867.
- Taylor G. J., Keil K., Berkley J. L., Lange D. E., Fodor R. V., and Fruland R. M. 1979. The Shaw meteorite: History of a chondrite consisting of impact-melted and metamorphic lithologies. *Geochimica et Cosmochimica Acta* 43:323–337.
- Tomioka N. and Fujino K. 1999. Akimotoite, (Mg, Fe)SiO<sub>3</sub>, a new silicate mineral of the ilmenite group in the Tenham chondrite. *American Mineralogist* 84:267–271.
- Troiano J., Rumble D. III, Rivers M. L., and Friedrich J. M. 2011. Compositions of three low-FeO ordinary chondrites: Indications of a common origin with the H chondrites. *Geochimica et Cosmochimica Acta* 75:6511–6519.
- Ulmer P. and Stalder R. 2001. The Mg(Fe)SiO<sub>3</sub> orthoenstatite-clinoenstatite transition at high pressures and temperatures determined by Raman-spectroscopy on quenched samples. *American Mineralogist* 86:1267–1274.
- Usselman T. M. 1975. Experimental approach to the state of the core; Part I, The liquidus relations of the Fe-rich portion of the Fe-Ni-S system from 30 to 100 kb. *American Journal of Science* 275:278–290.
- Wasson J. T., Rubin A. E., and Kallemeyn G. W. 1993. Reduction during metamorphism of four ordinary chondrites. *Geochimica et Cosmochimica Acta* 57:1867–1878.
- Weirich J. R., Wittman A., Isachsen C. E., Rumble D., Swindle T. D., and Kring D. A. 2010. The Ar-Ar age and petrology of Miller Range 05029: Evidence for a large impact in the early solar system. *Meteoritics & Planetary Science* 45:1868–1888.
- Weisberg M. K., McCoy T. J., and Krot A. N. 2006. Systematics and evaluation of meteorite classification. In *Meteorites and the early solar system II*, edited by Lauretta D. S. and McSween H. Y. Jr. Tucson: University of Arizona Press. pp. 19–52.
- Weisberg M. K., Smith C., Herd C., Haack H., Yamaguchi A., Chennaoui Aoudjenane H., Welzenbach L., and Grossman J. N. 2010. The Meteoritical Bulletin, No. 98. *Meteoritics & Planetary Science* 45:1530–1551.
- Wlotzka F. 1993. A weathering scale for the ordinary chondrites. *Meteoritics* 28:460.
- Woodcock N. H. 1977. Specification of fabric shapes using an eigen value method. *Geological Society of America Bulletin* 88:1231–1236.
- Woodcock N. H. and Naylor M. A. 1983. Randomness testing in three-dimensional orientation data. *Journal of Structural Geology* 5:539–548.

- Xie Z. and Sharp T. G. 2004. High-pressure phases in shock-induced melt veins of the Umbarger L6 chondrite: Constraints of shock pressure. *Meteoritics & Planetary Science* 39:2043–2054.
- Yamaguchi A., Scott E. R., and Keil K. 1998. Origin of unusual impact melt rocks, Yamato-790964 and-790143 (LL-chondrites). *Antarctic Meteorite Research* 11:18–31.
- Yamaguchi A., Scott E. R., and Keil K. 1999. Origin of a unique impact-melt rock, the L-chondrite Ramsdorf. *Meteoritics & Planetary Science* 34:49–59.
- Yang J., Goldstein J. I., Scott E. R. D., Michael J. R., Kotula P. G., Grimberg A., and Leya I. 2014. Thermal and collisional history of the Tishomingo iron meteorite: More evidence for early disruption of differentiated planetesimals. *Geochimica et Cosmochimica Acta* 124:34–53.

### SUPPORTING INFORMATION

Additional supporting information may be found in the online version of this article:

**Data S1:** Details on analytical methods.

**Table S1:**  $\mu$ CT parameters, sample details, and digitally extracted data.

**Table S2:** EBSD mapping parameters for the six largest maps of MIL 07273,12.

**Table S3:** EBSD data for larger ( $>5 \mu\text{m}$  diameter) olivine grains in five map sites.

**Table S4:** Inferences for high-temperature ( $T$  = temperature) time scales and cooling rates based on chemical variations in metal grains in MIL 07273, assuming low-pressure conditions.

**References S1.** References for Supporting Information.

---